Ore Geology Reviews 153 (2023) 105275

Contents lists available at ScienceDirect

Ore Geology Reviews

journal homepage: www.elsevier.com/locate/oregeorev

Distribution of critical metals in evolving pyrite from massive sulfide ores of the Iberian Pyrite Belt

Lola Yesares [a,*], Rubén Piña [a], José M. González-Jiménez [b], Reinaldo Sáez [c], Gabriel Ruíz de Almodóvar [c], Isabel Fanlo [d], Juan Manuel Pons [e], Raquel Vega [f]

[a] Departamento de Mineralogía y Petrología, Facultad de Ciencias Geológicas, Universidad Complutense de Madrid, C/José Antonio Novais, 12, Madrid 28040, Spain
[b] Instituto Andaluz de Ciencias de la Tierra, Consejo Superior de Investigaciones Científicas (CSIC)-Universidad de Granada, Avda. de las Palmeras 4, Armilla, Granada 18100, Spain
[c] Departamento de Ciencias de la Tierra, Universidad de Huelva, Huelva 21071, Spain
[d] Departamento de Ciencias de la Tierra, Cristalografía y Mineralogía, Universidad de Zaragoza, Pedro Cerbuna 12, Zaragoza 50009, Spain
[e] MATSA SAU, Almonaster la Real, Huelva 21342, Spain
[f] Atalaya Mining, Minas de Riotinto, Huelva 21660, Spain

ARTICLE INFO

Keywords:
Pyrite
VMS deposits
Trace elements
Electron backscatter diffraction (EBSD)
Iberian Pyrite Belt

ABSTRACT

With >90 known deposits containing original reserves of >2400 Mt of sulfide ore, the Iberian Pyrite Belt (IPB) is the largest volcanogenic massive sulfide (VMS) province on Earth. In these evolving mineral systems, texturally different pyrite exhibits characteristic mineralogy and trace element fingerprints. Pyrite (Py-1), which is well preserved in the polymetallic ores that crystallized at the earliest stage of VMS deposit formation, consists of kernels of pyrite framboids surrounded by concentric colloform bands and ended by faceted outlines. It is rich in some metals like Pb, Zn, Sb and As (mostly hosted as nano-to-micron-sized particles, including galena, tetrahedrite and arsenopyrite) but depleted in Cu, Co and Bi. In contrast, pyrite from the pyritic and Cu-rich ore overprinted by late fluids exhibits spongy-looking (Py-2) or homogenous (Py-3) cores surrounded by external facets with crystallographic continuity across the whole single grains due to re-crystallization. Py-2 is depleted in most trace elements with the exception of Au and Bi, which occur both in solid solutions and as nano-to-micron-sized inclusions. Py-3 has the highest Cu, Ag, Co and Ni (mainly associated to nano-to-micron-sized particles of tennantite, chalcopyrite and gersdorffite) and the lowest Au contents in the form of native gold. The progressive increase in metal contents from inner to outer parts of Py-1 matches with the onset of the economic metal endowment of VMS deposits in the IPB, whereas Py-2 and Py-3 are associated with metal shoot processes that led to both leached and high-grade ores, very likely when mafic rocks were emplaced into the footwall of the deposits.

1. Introduction

Volcanogenic massive sulfide (VMS) deposits are stratiform exhalative and/or replacive ore bodies, formed from hydrothermal fluids discharging at/or near the seafloor and are typically associated with volcanic and/or sedimentary rocks (Galley et al., 2007). These types of deposits, which have been formed throughout most of Earth history from the Archean to present day (Hannington et al., 1995; Maslennikov et al., 2017; Grant et al., 2018), are typically underlain by discordant stockwork mineralization interpreted as the feeder pathways for mineralizing fluids (Solomon, 1976; Lydon, 1988; Large, 1992; Piercey, 2011). Fossil VMS are of particular interest as they are among the Earth's main sources for base metals (i.e., Cu, Pb, Zn; Franklin et al., 1981; Franklin et al., 2005; Galley et al., 2007; Hannington, 2014) essential for the industry of many developed countries (e.g., European Commision, 2020; U.S. Geological Survey, 2022). In addition, VMS have potential to produce as by-products other valuable metals considered as critical for many countries, including Au, Ag, Co, Ni, Mn, Cd, In, Sn, Se, Bi, Te, Ga, Ge, Sb and Ba (Huston and Large 1989; Wang et al., 1999; Galley et al., 2007; Mercier-Langevin et al., 2011; Wright et al., 2016; Torró et al., 2022).

VMS are typically constituted by pyrite, chalcopyrite, galena, pyrrhotite, sphalerite and tetrahedrite-tennantite, all of which can host minor and trace elements structurally bounded or as micro/nano-sized

* Corresponding author.
E-mail address: myesares@ucm.es (L. Yesares).

https://doi.org/10.1016/j.oregeorev.2022.105275
Received 6 October 2022; Received in revised form 21 December 2022; Accepted 26 December 2022
Available online 29 December 2022

mineral inclusions (McClenaghan et al., 2004; McClenaghan et al., 2009; Maslennikov et al., 2009; Deditius et al., 2011, 2014; Yesares, 2019; Wright et al., 2016; Makvandi et al., 2016; Dehnavi et al., 2018). However, their interplay during the genesis and evolution of this type of deposits is still poorly constrained. This mineralogical site of trace metals can now be addressed more precisely through a number of mineral microanalysis techniques such as electron probe microanalysis (EPMA), scanning electron microscope (SEM), laser ablation inductively coupled plasma mass spectrometry (LA-ICP-MS), secondary-ion mass spectrometry (SIMS), and high-resolution transmission electron microscopy (HRTEM).

Efforts in the study of pyrite, the most abundant mineral in VMS deposits, have shown that it forms under a wide range of temperatures and physico-chemical conditions (Franklin et al., 1981; Franklin et al., 2005; Lydon 1988 Galley et al., 2007), upon which it can bear specific suites of minor and major elements (e.g., Maslennikov et al., 2009; Genna and Gaboury, 2015). The available works on the matter seemingly suggest that pyrite that formed during the earliest stages of formation of the VMS (e.g., framboid, colloform and spongy-like relicts) is usually enriched in elements that are typically transported by low-to-moderate temperature hydrothermal fluids (i.e., Ag, Sb, Ni). In contrast, pyrite that originated during later stages of the evolution of the hydrothermal system are usually affected by recrystallization and/or annealing and depleted in minor and trace element in general (Auclair et al., 1987; McClenaghan et al., 2004; Layton-Matthews et al., 2008; Revan et al., 2014; Genna and Gaboury, 2015; Dehnavi et al 2018; Grant et al., 2018; Yuan et al., 2018; Wang et al., 2021).

This study aims to improve our current knowledge on how critical metals are concentrated in pyrite from VMS deposits by analyzing a suite of spatially and paragenetically well-constrained massive sulfide ores from two deposits from the Iberian Pyrite Belt (i.e., Masa Valverde and La Magdalena). To do that, we have selected pyrite-bearing ore deposited during the early stages of VMS formation (i.e., Zn + Pb distal lenses originated from fluids up to 250 °C in black shales from the Masa Valverde deposit), and compared them with those deposited during the latest hydrothermal overprint (i.e., pyritic and Cu-rich inner lenses hosted by rhyodacites but precipitated from fluids up to 400 °C from La Magdalena deposit), as reported by Almodóvar et al. (2019). Previous works on VMS deposits from the IPB have shown significant concentrations of precious metals (Au and PGE) in whole-rock samples (Marcoux et al., 1996; Leistel et al., 1998; Pašava et al., 2007; Barret et al., 2008; Oliveira et al., 2011; Yesares et al., 2015) as well as other economically interesting (semi)-metals such as Cu, Zn, Ni, Bi, Co, In, Ga, Ge, In and Sn (Almodóvar et al., 1998). EPMA data in pyrite from Neves Corvo (Serrati et al., 2002; Gaspar, 2002) and LA-ICP-MS data in pyrite from Tharsis (e.g., Conde et al., 2020) show erratic variations in the contents of Cu, Zn, Pb, Ag, Sn, Se, Sb and As. However, none of these studies have thoroughly linked the distribution of trace elements in relation to the textural maturation of pyrite or the genetic evolution of the deposits.

In this manuscript, we integrate data generated by EPMA, field emission scanning electron microscope (FESEM), electron backscattered diffraction (EBSD) and LA-ICP-MS on pyrite grains from two VMS deposits located in the IPB. These new data illustrate the metal incorporation in pyrite during mineral system evolution, which elaborates into the characterization of the sources for and mechanisms of metal enrichment in VMS deposits at the IPB and elsewhere. In turn, this insight bears implications for the metallurgical beneficiation of pyrite-rich VMS ore.

2. Geological background

The Iberian Pyrite Belt (IPB) is the Earth's largest cluster of volcanogenic massive sulfide deposits and is located at the southwestern part of the Iberian Peninsula. The IPB is one of three domains making up the South Portuguese zone, which is the southernmost zone of the Iberian Hercynian Massif (Carvalho, 1976). The stratigraphic succession of the IPB is composed of sedimentary and igneous rocks of Middle Devonian–Pennsylvanian age and they comprise three main lithostratigraphic units. From the footwall to the hanging wall, these are the Givetian–Famennian pre-volcanic Phyllite–Quartzite Group, the late-Famennian–early Visean Volcano–Sedimentary Complex, and the Visean–Bashkirian post-volcanic Culm Group (Schermerhorn, 1971).

All lithostographic units, including the VMS deposits, were affected by transpressional deformation during the Variscan orogeny, resulting in thin-skinned deformation defined by imbricate thrust panels, folding, and very low-grade metamorphism (Silva et al., 1990). At deposit scale, the strain was focused into the base metal-rich part of the massive sulfide orebodies, thus favoring the detachment and stacking of massive sulfide slices. Moreover, from tectonic thickening and the resulting accumulation of tonnage, this process may have also changed the base metal grade distribution in the deposits, which would have resulted in localized higher or lower grades than those in their original distribution (Castroviejo and Quesada, 2011).

Massive sulfide deposits from the IPB are hosted by sedimentary, volcanic and volcanoclastic strata (Schermerhorn, 1971; Sáez et al., 1999; Leistel et al., 1998: Almodóvar et al., 1998). The most common host lithologies are black shales in the south (e.g., Masa Valverde, Tharsis, Las Cruces, Aznalcóllar and Frailes) and felsic volcanic and volcanoclastic rocks in the north (e.g., La Magdalena, Aguas Teñidas, Riotionto, Lomero-Poyatos, Cueva de la Mora, Sotiel-Coronada, Migollas and San Miguel) (Fig. 1).

Ore mineralogy of VMS deposits from the IPB consists mainly of pyrite, with subordinate amounts, in decreasing order of abundance, of sphalerite, galena, chalcopyrite, tennantite-tetrahedrite and arsenopyrite. Many other minor phases have also been identified including Bi- and Pb-sulfosalts, cassiterite, magnetite, stannite, electrum and cobaltite (García de Miguel, 1990; Marcoux et al., 1996; Almodóvar et al., 1998; Yesares et al., 2015).

The deposits in which this study is based are Masa Valverde and La Magdalena. The Masa Valverde deposit (Ruiz et al., 2002; Atalaya Mining press release, 2021) is located in the southern IPB, within the southern flank of the Valverde del Camino anticline, and beneath the Culm Group sedimentary rocks, which extends into the western part of the anticline (Fig. 1). It is currently being explored by Atalaya Mining and includes known inferred reserves of 31 Mt of polymetallic ore at 3 % Zn, 1.2 % Pb, 40 g/t Ag and 0.7 g/t Au, and 19 Mt of Cu-rich ore at 0.7 % Cu, 0.9 % Zn, 0.9 % Pb, 41 g/t Ag and 0.8 g/t Au. This VMS deposit is hosted by a thick sequence of black shales and felsic volcaniclastic rocks from the Volcanic-Sedimentary Complex. The deposit extends >1.3 km long, up to 200 m wide and plunges 30° NW from a depth of approximately 430 m to no <800 m. It is made up of two massive sulfide bodies separated by a stockwork zone that can exceed 100 m in thickness. The largest orebody ranges from a few to 70 m in thickness and consists of lenses of massive sulfides interbedded with tuffs and shales. Although the smaller orebody is thinner, drilling is underway and the geological relationships between the two orebodies are still poorly understood. The mineral distribution in the ore bodies is very irregular and includes barren pyrite, polymetallic (Zn + Pb), and minor Cu-rich facies.

The La Magdalena deposit (Granda-Sanz et al., 2019) is located in the northern IPB (Fig. 1). It is currently mined by Minas de Aguas Teñidas S. A.U. (MATSA) and constitutes the largest discovery in the IPB in recent decades, including >40 Mt reserves of high grade polymetallic and cupriferous ores. The deposit consists of two ore bodies (the upper ore body is 90 m thick and the deeper ore body is ~750 m thick) hosted by a thick sequence of the Volcanic-Sedimentary Complex, which in this area is mainly constituted of felsic volcanoclastic rocks and minor black shales. Collectively, these ore bodies are over 1.8 km long and up to 900 m wide, and plunge 75° N from a depth of ~225 m. A striking feature is the spatial association of mafic sills at the footwall of the La Magdalena deposit. These mafic intrusions lack the typical hydrothermal alteration at the footwall of the deposits, but display the distinctive shearing and

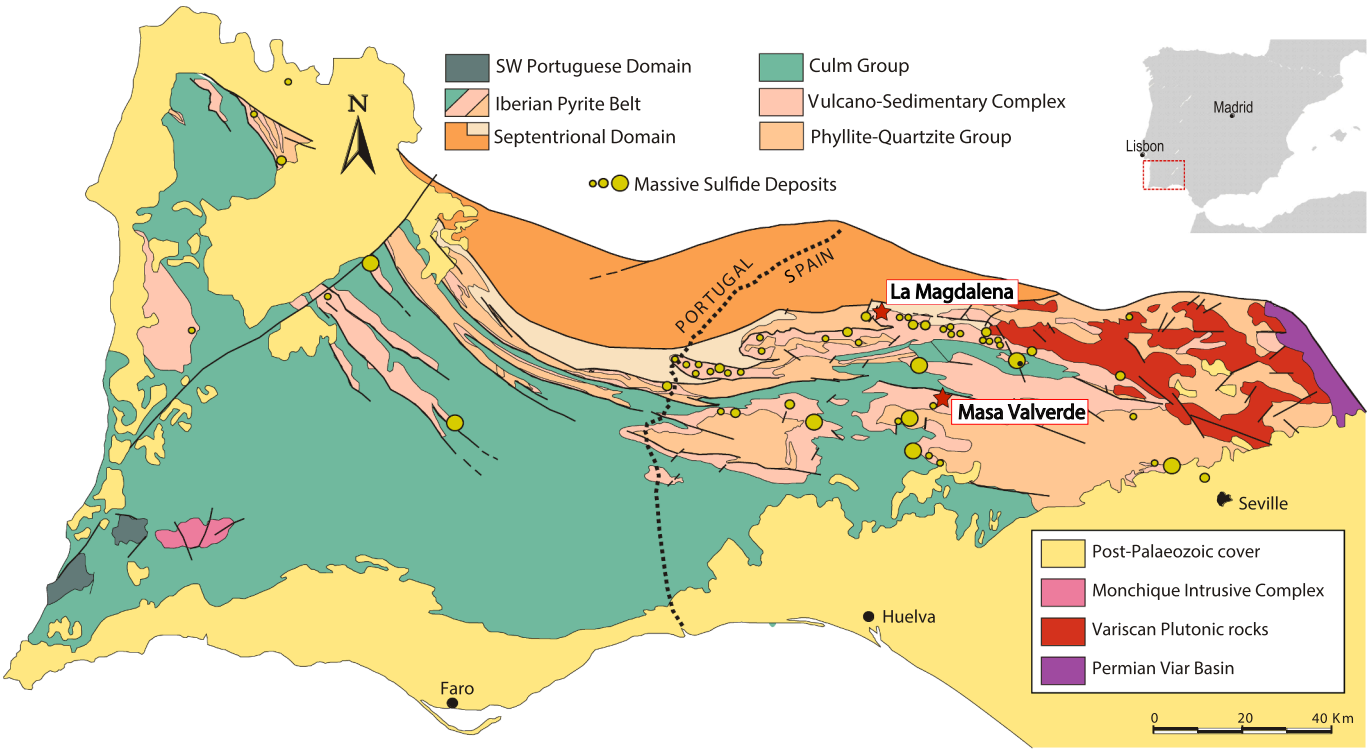

Fig. 1. Geologic map of the South Portuguese Zone, including the location of the VMS deposits from the IPB selected for this study. The diameter of the yellow circles is related to the size of the deposits. (modified from Sáez, 2010). (For interpretation of the references to color in this figure legend, the reader is referred to the web version of this article.)

folding consistent with the structure of the Variscan Orogeny in the area. Therefore, mafic intrusions were emplaced at the footwall of the La Magdalena deposit after the formation of the VMS but before regional metamorphism.

3. Analytical methods

Mineralized samples of drill-cores from both Masa Valverde and La Magdalena deposits were prepared as polished thin sections for petrographic study by transmitted and reflected light optical microscopy in order to characterize the ore mineralogy and textures, with special focus on the different textural pyrite types. These are representative of the most common features identified in the IPB among hundreds of samples that we have previously studied in many deposits from the IPB (i.e., Almodóvar et al., 1998; Almodóvar et al., 2019; Sáez et al., 2011; Yesares et al., 2015; Yesares, 2019).

3.1. Field emission scanning electron microscopy (FE-SEM)

Detailed mineralogical and textural studies were performed by using: 1) a SEM FEI-QUANTA 200 equipped with an energy dispersive X-ray spectroscopy (EDAX) microanalyzer Genesis 2000 at the Servicios Centrales de Investigación of the University of Huelva, Spain; and 2) (FE-SEM) coupled with an energy dispersive spectra (EDS) using a Leo Gemini equipment available at the Centro de Instrumentación Científica of the University of Granada, Spain. In both cases, accelerating voltage was 20 kV with a beam current optimized for each EDAX or EDS analysis.

3.2. Electron probe microalalyzer (EPMA)

The major and minor element compositions of the different pyrite types were analyzed using two EPMA equipment: (1) JEOL JXA-8230 at the Centres Científics i Tecnològics of the University of Barcelona; and (2) a JEOL JXA-8200 super probe at the University of Huelva, Spain. The measurements were performed on carbon-coated polished sections using an accelerating voltage of 20 kV, with 20nA beam current, 30 s counting time for the peaks and 10 s for the background measurements. Single spot and line analyses were carried out on inclusion free areas previously selected using backscattered electron (BSE) images. Concentrations of S, Fe, Cu, Zn, Co, Ni, Cd, Pb, Au, Ag, Hg, Bi, As, Sb, Se in pyrite were determined by wavelength-dispersive spectroscopy (WDS). Routine data reduction, including full matrix (ZAF) corrections, were performed. The X-ray lines employed were Kα for S, Co, Fe, Ni, Cu and Zn; Mα for Hg, Au, Pb and Bi; Lα for As, Ag, Se and Sb; and Lβ for Cd. The standard materials for the EMPA analysed were: S (FeS2), Fe (FeS_2), Cu (Cu), Zn (ZnS), Co (Co), Ni (Ni), Cd (CdTe), Pb (PbS), Au (Au), Ag (Ag), Hg (HgTe), Bi (Bi_2S_2), As (Zn_3As_2), Sb (Sb_2S_3), Se (SnSe).

3.3. Electron backscatter diffraction (EBSD)

Mineral fabric and crystallographic orientation of pyrite grains were measured on thin sections, previously chemically polished by colloidal silica (50 nm), using two FE-SEM model Carl Zeiss SMT available at the Centro de Instrumentation Científica (CIC) of the University of Granada and the Servicio General de Apoyo a la Investigación-SAI from the University of Zaragoza, Spain. The EBSD patterns were generated by the interaction of a vertical incident electron beam with a polished thin section, tilted 70° to the horizontal in the FE-SEM. The measurements were conducted with an accelerating voltage of 20 to 25 kV and working distance of 1.0–15.0 mm. The diffraction patterns were projected onto a phosphor screen and recorded using a digital coupled charge dispositive (CCD) camera. The resulting image was then processed and indexed using the AZTEC software distributed by Oxford Instruments. Maps were acquired with sampling step size of 0.2 to 1.5 μm depending on the mean grain size. Post-acquisition processing was carried out using the CHANNEL5 software distributed by Oxford Instruments, including the extrapolation of well-indexed neighbouring points to non-indexed

points, and removal of grains (as defined by continuous domains characterized by an internal misorientation of 10°) smaller than 5 pixels in average diameter. We present the resulting data in the form of color-coded maps and pole figures. For the maps that show crystal orientation changes relative to the specific direction of the sample reference frame, full red, green, and blue colors are assigned to the grains whose {100}, {110} or {111} set of planes are parallel to the projection of the inverse pole figure. Intermediate orientations are colored as a mixture of the primary axes.

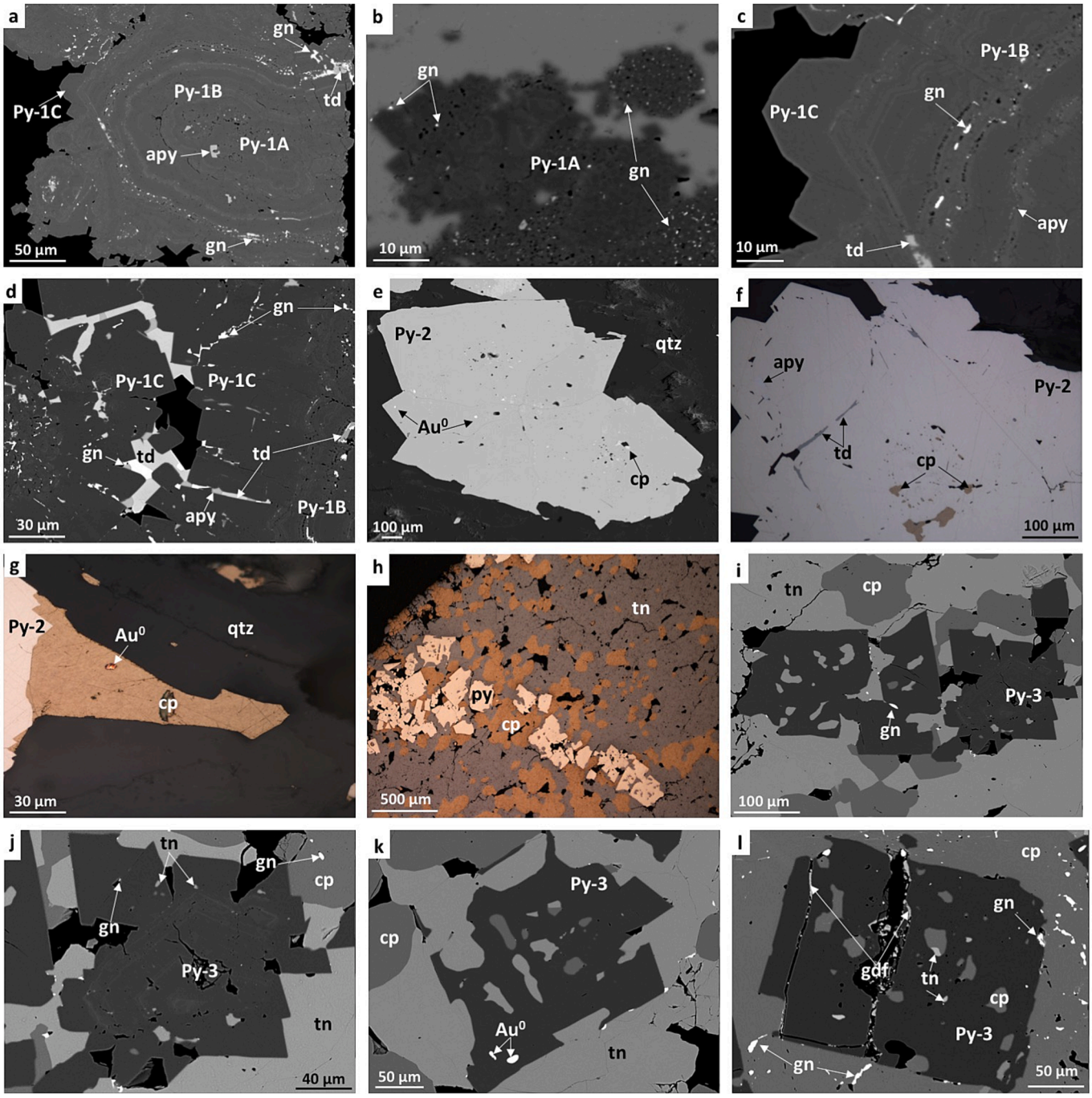

Fig. 2. Reflected light and BSE images of different pyrite types from polymetallic (Masa Valverde) and Cu-rich (La Magdalena) of the IPB. (a) Py-1 consists of framboids relicts (Py-1A) in the cores surrounded by concentric colloform bands (Py-1B) ended by faceted outlines (Py-1C). Note that Py-1 includes subhedral arsenopyrite (apy) sealing open spaces in Py-1A but galena (gn) and tetrahedrite (td) occur within Py-1B concentric layers. (b) Fine galena micron-sized inclusions in the framboidal pyrite of Py-1A. (c) Micron-sized inclusions of galena and arsenopyrite oriented parallel to colloform pyrite concentric layers and tetrahedrite lining interstices between Py-1B bands. (d) galena, tetrahedrite and arsenopyrite lining open spaces in the outer faceted rims of Py-1C. (e, f) Euhedral pyrite with spongy cores (Py-2). Note that chalcopyrite (cp) and tetrahedrite inclusions are mainly filling interstices in spongy cores whereas inclusions of arsenopyrite and native gold (Au) are mainly concentrated towards outer rims. (g) native gold particle included in chalcopyrite intergrown with Py-2. (h, l) Euhedral pyrite (Py-3) included in a matrix formed by an intergrowth of chalcopyrite and tennantite (tn). (j) Detail of the euhedral pyrite showing As-rich zoned cores and, galena and tennantite inclusions. (k) Tennantite, chalcopyrite and native gold replacing euhedral pyrite. (l) Gersdorffite (gdf) lining late fractures in Py-3 Tennantite, chalcopyrite and galena are also observed replacing Py-3.

3.4. Laser ablation inductively coupled plasma mass spectrometry (LA-ICP-MS)

Trace element concentrations on different textured pyrite were measured by LA-ICP-MS at the LabMaTer of the Université du Quebec à Chicoutimi, Canada. Samples were analyzed using an Excimer 193-nm Resolution M−50 laser ablation system equipped with a double volume cell S-155 and coupled with an Agilent 7900 mass spectrometer. The ^{34}S, ^{54}Fe, ^{57}Fe, ^{59}Co, ^{60}Ni, ^{65}Cu, ^{66}Zn, ^{75}As, ^{107}Ag, ^{121}Sb, ^{197}Au, ^{208}Pb, and ^{209}Bi isotopes were monitored. The purpose of monitoring Si was to ensure that no silicates were included in the analyses. Single spot LA-ICP-MS analyses were carried out on pyrite free of inclusions, as previously identified under FE-SEM. Individual analyses were made using a laser beam size ranging between 11 and 55 μm, a laser frequency of 15 Hz, and a fluence of 3 J/cm^2. An argon-helium gas mix was used as carrier gas. The gas blank was measured during 30 s before switching on the laser for 60 s. The ablated material was then analyzed using the mass spectrometer in time resolution mode using mass jumping and a dwell time of 10 ms/peak. Data reduction was carried out by the Iolite package of Igor Pro 8.0 software (Patton et al. 2011). Internal standardization was based on ^{57}Fe by using the iron contents determined by EPMA. During data screening, the entirety of the laser signal of inclusion-free areas was integrated. We used the certified reference material MASS-1 for the calibration of trace elements. It consists of a Zn-Cu-Fe-S pressed powder pellet provided by USGS and doped with 50–70 ppm of most chalcophile elements. The calibrations were monitored using GSE-1 g and UQAC-FeS1. GSE-1 g is a natural basaltic glass provided by the USGS doped with most elements at 300–500 ppm, and UQAC-FeS1 is an in-house Fe-S reference material doped with trace amounts of most chalcophile elements. Analyses of these materials agree well with the certified and working values are found in Appendix 1. Element distribution maps in selected pyrite grains were performed using a laser frequency of 15 Hz and a power of 3 J/cm^2. Beam size and stage movement speed were variable in each map (ranging from 11 to 19 μm and 15 to 20

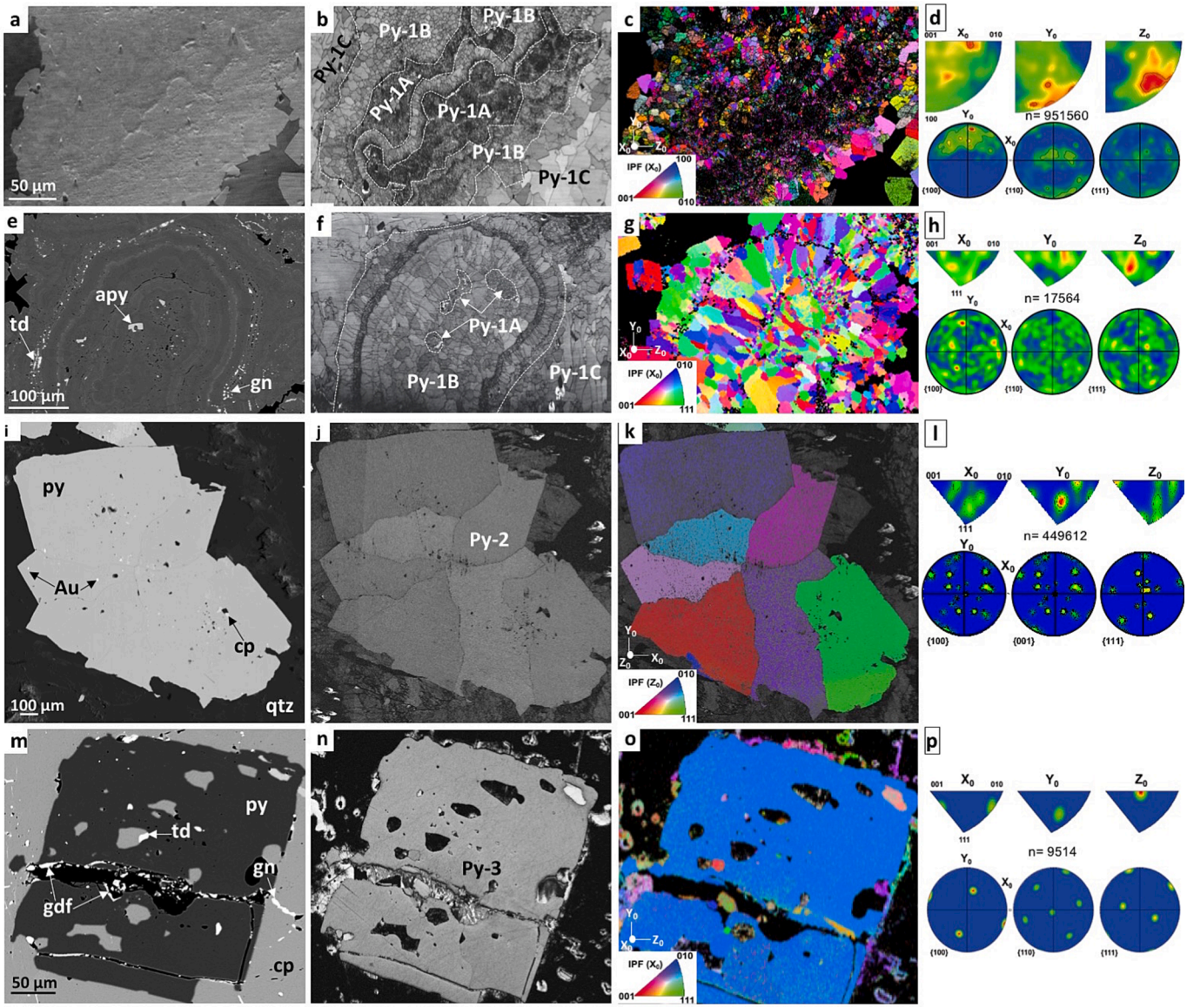

Fig. 3. BSE images and corresponding EBSD maps of the selected pyrite types analyzed in this study, including primary Py-1 (a-h), and euhedral Py-2 (i-l) and Py-3 (m-p). b, f, j and n are orientation contrast map showing different grey scale changes in crystallographic orientation are shown in images; dark areas are grain boundaries, holes and fractures. c, g, k and o show inverse pole figure (IPF) maps showing different orientations in colors relative to the X0 direction. Distribution of crystallographic preferred orientation (CPO) data of pyrite in the corresponding areas are presented relative to sample coordinates (X, Y, Z) and pyrite {1 0 0}, {0 0 1} {1 1 0} and {1 1 1} pole. Note that data are one point per grain data, smoothed with a Gaussian fit half-width and presented on upper-hemisphere equal-area pole figure. Colors are the same as in all images.

μm/s, respectively) to optimize the spatial resolution and analyses time of the areas mapped. Maps were generated using the Iolite software in the mode of time-resolved composition of each element, and showing the semiquantitative concentration of the element.

4. Petrography

Three types of pyrite are present in the studied samples (Fig. 2a-l and Fig. 3a-p). Type 1 pyrite (Py-1) is very common in the polymetallic ores, whereas Type 2 (Py-2) and Type 3 (Py-3) are more frequent in both cupriferous ores and in mineralization affected by high-temperature hydrothermal overprint.

Py-1 is colloform-textured and consists of cores with multiple pitted spherical aggregates resembling pyrite framboids (Py-1A; Fig. 2a-c), which are surrounded by discrete pyrite layers with local inclusions of galena, tetrahedrite, arsenopyrite and sphalerite, found between layers or occasionally associated to pores (Fig. 2a-d; Fig. 3b and f). The band contrast (BC) EBSD maps are consistent with FESEM observations and confirm that colloform pyrite consists of concentric colloform layers with kernels of pyrite framboids. At detail, the cores of colloform pyrite are formed by micro-granular pyrite crystals that are randomly distributed (Fig. 3b-c and f-g). In contrast, BC mapping of the outer layers reveal: (1) radial pyrite crystals (i.e., acicular and/or elongated) that are implanted perpendicularly to colloform layering upon Py-1A, and (2) granular grains with a range of morphologies (Py-1B). Granular microcrystals of Py-1A are nearly equigranular and subhedral/euhedral whereas acicular, elongated and granular crystals in the layers (Py-1B) are strongly inequigranular and coarsening outwards (Fig. 3b-c and f-g). The largest crystals in the outermost layering (Py-1C) tend to exhibit grew on granular grains of Py-1B exhibiting well-developed facets outwards (Fig. 3b-c and f-g). The EBSD inverse pole maps show no significant crystal bending within single pyrite crystals (either acicular, elongated or granular) either in cores or concentric layers (Fig. 3c and g), thus lacking any significant crystal-plastic deformation. However, the inverse pole diagrams illustrate that the colloform polycrystalline aggregates have coexisting undefined and well-developed crystallographic preferred orientation (CPO) (Fig. 3d and h). The scattered pole distribution can be attributed to granular pyrite crystals with different orientations in the cores and some of the colloform layers. Well-developed bulk CPO marked by a preferential clustering of {100} and ⟨100⟩ directions in the pole diagrams is due to the preferential orientation of pyrite in the outer layers. Particularly, the preferential clustering of {100} poles in the upper right quadrant in Fig. 3d and ⟨100⟩ in the upper right and bottom left quadrants of the pole diagram shown in Fig. 3d identifies the coarse-faceted crystals of Py1-C. In contrast, clusters of {100} in all the quadrants of the pole figure shown in Fig. 3h may be attributed to the preferential orientation of acicular and elongated crystals in radial aggregates of Py-1B shown in Fig. 3g.

Py-2 consists of coarser pyrite grains than Py-1 (1.5 to 2 mm in diameter) with spongy cores and faceted outlines (Fig. 2e-g). The BC image reveals that such euhedral terminated pyrite crystals with spongy cores show a core-to-rim crystal continuity, with no appreciable differences in the orientation between the spongy-looking core and the inclusion-free rim. Rather, pyrite clusters are constituted by blocky aggregates (Fig. 3j), which consist of at least seven individual subgrain domains (Fig. 3k) with their own different CPO according with the ⟨100⟩ and ⟨001⟩ axes (Fig. 3l).

Py-3 also includes coarse grains with perfectly well developed external facets and homogenous internal microstructure (Fig. 2h-I and 3 m). Consistently, the grey-scale BC images do not reveal appreciable differences in crystallographic orientation across single grains (Fig. 3n) which also accords well with both the very homogenous colour distribution in the inverse figure maps (Fig. 3o) and very simple pattern of clustering of poles in the pole figure plot (Fig. 3p).

5. Mineral inclusions in pyrites

A combination of FE-SEM, EPMA and LA-ICP-MS maps (Figs. 2, 4 and 5) shows that pores of framboidal Py-1A are commonly filled by tiny (<1 μm) galena inclusions (Fig. 2b) or arsenopyrite (up to 10 μm) (Fig. 2a, Fig. 4a and Fig. 5a). Py-1B concentric layers contain mostly anhedral galena (<5 μm) and minor arsenopyrite (<0.5 μm) particles that grew parallel to the colloform Py-1B bands (Fig. 2a, c, Fig. 4a and Fig. 5a), whereas tetrahedrite is coarser grained (>10 μm), irregular in shape, and found in the interstices between radial crystals of the colloform Py-1B (Fig. 2a, c, Fig. 4a). Faceted Py-1C also hosts galena (<25 μm), tetrahedrite (<50 μm), and arsenopyrite (<20 μm), whose abundance and grain size increase outwards (Fig. 2d). It is worth to note that euhedral Py-1C is devoid of fine-grained mineral sulfide or sulfosalt inclusions. These petrographic observations are consistent with the LA-ICP-MS line-profile time-resolved spectras for Py-1, which show flat patterns for most of the analyzed elements except for local spikes of Pb, Cu and As (Fig. 6a and b) attributed to the ablation of galena, tetrahedrite and arsenopyrite.

Py-2 is commonly poor in inclusions, although it contains some observable particles of chalcopyrite, tetrahedrite, arsenopyrite and native gold (Fig. 2e, f, g, Fig. 4b and Fig. 5b). FESEM imaging, EPMA and LA-ICP-MS maps show porous cores of Py-2 with inclusions of chalcopyrite and tetrahedrite (up 30 μm across) (Fig. 2e, f and Fig. 4b), and Py-2 rims hosting arsenopyrite (>40 μm) and native gold (<5 μm in diameter) (Fig. 2e, f and Fig. 5b). Line-profile time-resolved spectra acquired by LA-ICP-MS for Py-2 are consistent with these observations, showing smooth core-to-rim profiles of Cu and Zn (Fig. 6c) but local spikes of ^{75}As, ^{209}Bi, ^{208}Pb, ^{65}Cu and ^{197}Au (Fig. 6d) attributed to ablation of arsenopyrite, tetrahedrite, galena, chalcopyrite and native gold particles.

Py-3 contains chalcopyrite, tennantite, galena, gersdorffite and native gold inclusions (Fig. 2h-l, Fig. 4c and Fig. 5c). Tennantite and chalcopyrite are the most abundant minerals in inclusions and the largest grains (~50 μm). Their concentrations are similar in either Py-3 cores or rims (Fig. 2i-k). Gersdorffite forms tiny crystals (~10 μm) filling late fractures in Py-3 (Fig. 2l). Galena and native gold inclusions are ~20–30 μm, and are randomly distributed across the Py-3 grains (Fig. 2i, j and k). Some line-profile LA-ICP-MS spectra on Py-3 display spiked and irregular pattern for most elements in these inclusions (Cu, As, Pb) as well as other base (Zn, Bi, Co) and precious (Au, Ag) metals (Fig. 6e and f), suggesting the presence of inclusions at depth.

6. Major, minor and trace element fingerprints of pyrite types

Pyrite analyzed in this study is As-rich (up to 3.69 wt%), with Fe in the range between 43.7 and 46.91 wt% and S between 49.04 and 53.72 wt% (Appendix 2). Inclusion-free areas have highly variable contents of minor and trace element (Fig. 7 and Appendix 3), with maximum values of 25,400 ppm Cu, 25,300 ppm Zn, 15,100 ppm Pb, 9,600 ppm Sb, 890 ppm Ag, 520 ppm Bi, 240 ppm Ni, 72 ppm Co and 39 ppm Au.

Py-1 contains the highest average contents of As (20,034 ppm), Zn (5,996 ppm), Pb (2,207 ppm) and Sb (1,667 ppm), but the lowest for Bi (0.08 ppm), Co (0.3 ppm) and Cu (688 ppm) (Fig. 7 and Appendix 3), with positive correlations between Au and As, and Ag and As + Sb (Fig. 8a and b). Py-1A has higher Sb (up to 7000 ppm), Pb (up to 5000 ppm, Ni (up to 147 ppm), Au (up to 7 ppm), and lower As (up to 28,800 ppm), Zn (up to 10,300 ppm) and Cu (up to 750 ppm) (Fig. 7 and Appendix 3) than Py-1B and Py-1C. Py-1B is uniquely rich in As (up to 44,000 ppm) (Fig. 7 and Appendix 3), whereas euhedral Py-1C is relatively rich in Cu (up to 3290 ppm) and Zn (up to 25,300 ppm) but poor in Pb (up to 3500 ppm), Sb (up to 880 ppm), Ni (up to 72) and Au (up to 4 ppm) relative to Py-1A and Py-1B (Fig. 7 and Appendix 3).

Py-2 shows the lowest average contents of Pb (448 ppm), Sb (267 ppm), As (100 ppm), Zn (69 ppm) and Ag (19 ppm), but the highest Au (5 ppm) and Bi (36 ppm) concentrations (Fig. 7 and Appendix 3). There

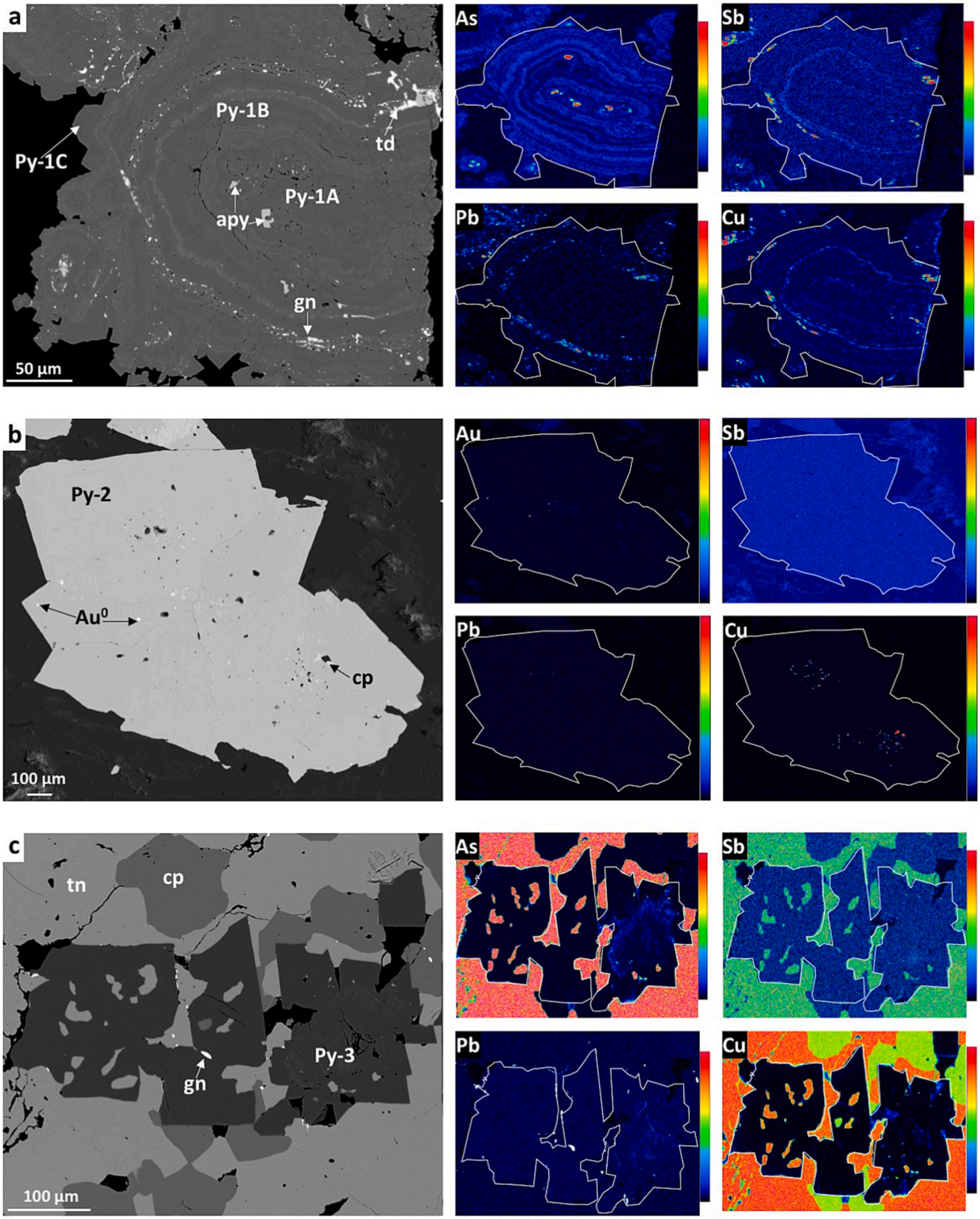

Fig. 4. WDS X-ray EPMA elemental maps and the corresponding BSE images of selected pyrite grains analyzed in this study. (a) As, Sb, Pb and Cu maps on Py-1 illustrating the presence of discrete inclusions of arsenopyrite (apy), tetrahedrite (td) and galena (gn). (b) Au, Sb, Pb and Cu maps of Py-2 with native gold and chalcopyrite (cp) inclusions. (c) As, Sb, Pb and Cu maps illustrating chemical variation in Py-3 and chalcopyrite, tennantite (tn) and galena inclusions.

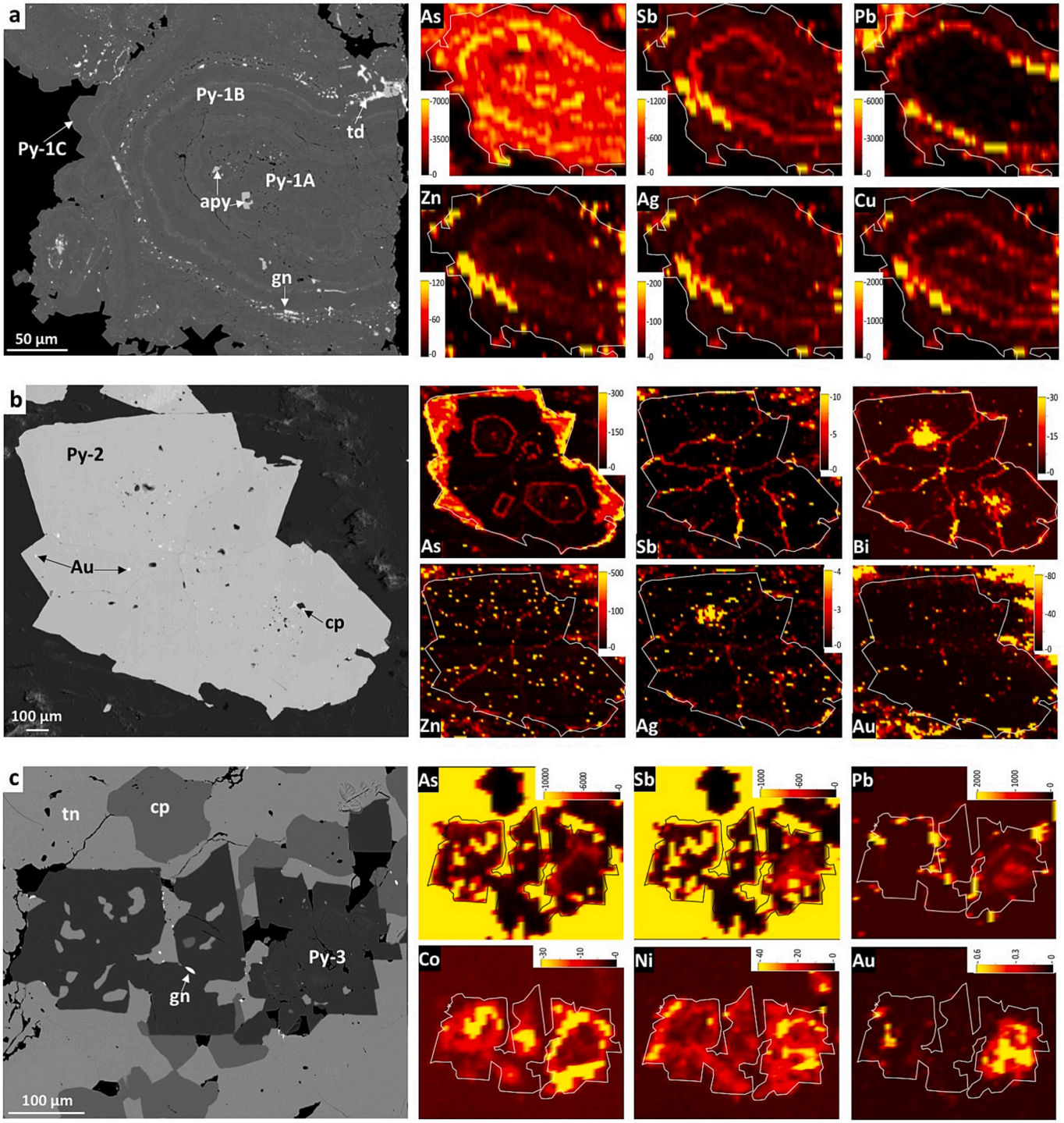

Fig. 5. LA-ICP-MS elemental maps and the corresponding BSE images of selected pyrite grains analyzed in this study. (a) As, Sb, Pb, Zn, Ag and Cu distributions in Py-1. (b) As, Sb, Bi, Zn, Ag and Au distribution in Py-2. (c) As, Sb, Pb, Co, Ni and Au zoning in euhedral Py-3. Semiquantitative concentrations are given in ppm within the scale-bar inset.

are overall positive correlations between the following elements: Ag vs As + Sb, Ag vs Pb, Au vs Zn + Pb, Cu vs Zn + Pb, Ni vs Co, Au vs Ni + Co, and Au vs Bi (Fig. 8b-h). Spongy-looking cores of Py-2 are richer in Pb (up to 15,100 ppm), Cu (up to 14,200 ppm), Zn (up to 1,480 ppm), Sb (up to 664 ppm), Ag (up to 540 ppm), Co (up to 26 ppm) and Bi (up to 520 ppm) relative to their outer rims (Appendix 3, Fig. 4b and Fig. 5b).

Py-3 has the highest average values of Cu (8,566 ppm), Ag (135 ppm), Ni (84 ppm) and Co (31 ppm) but the lowest in Au (1 ppm) relative to the other pyrite types, although it is also rich in As (14,229), Zn (2006 ppm), Sb (1570 ppm) and Pb (1460 ppm) (Fig. 7 and Appendix 3). Py-3 shows positive correlation between Ag vs As + Sb, Au vs Zn + Pb, Cu vs Zn + Pb and Au vs Bi (Fig. 8b, d, e and h); the cores of Py-3 are rich in As (up to 55,000 ppm), Pb (up to 10,500 ppm), Sb (up to 9500 ppm), Ni (up to 240 ppm) and Au (up to 3 ppm) relative to their surrounding rims (Appendix 3 and Fig. 4c and Fig. 5c).

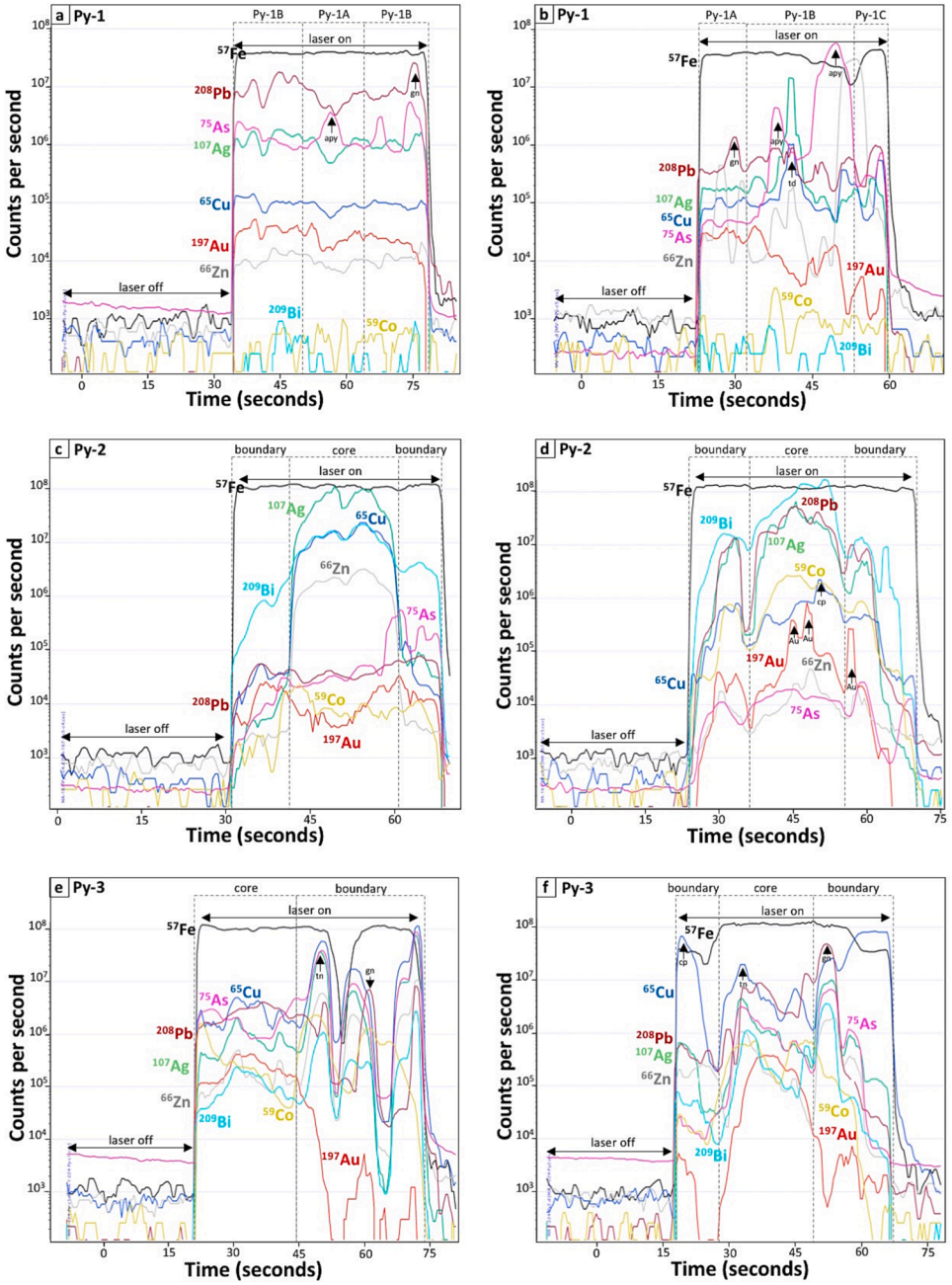

Fig. 6. Representative time-resolved LA-ICP-MS spectra collected during trace element analyses of Py-1 (a–b), Py-2 (c–d) and Py-3 (e–f). The transient spectra show both homogenous signals indicating elements in solid solution or particles not identified in this study (a and c) and spikes profiles suggesting the presence of micron-sized particles (b, d, e and f).

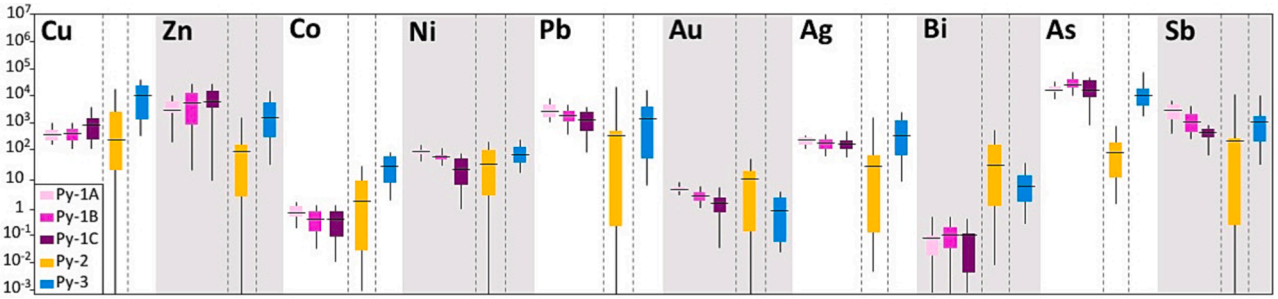

Fig. 7. Concentration of minor and trace elements in different textural pyrite types represented as box plot. Only inclusion-free LA-ICP MS analysis data were included in this plot (n = 133). Data are plotted ppm on a vertical logarithmic scale, including minimum, median and maximum values for each single element.

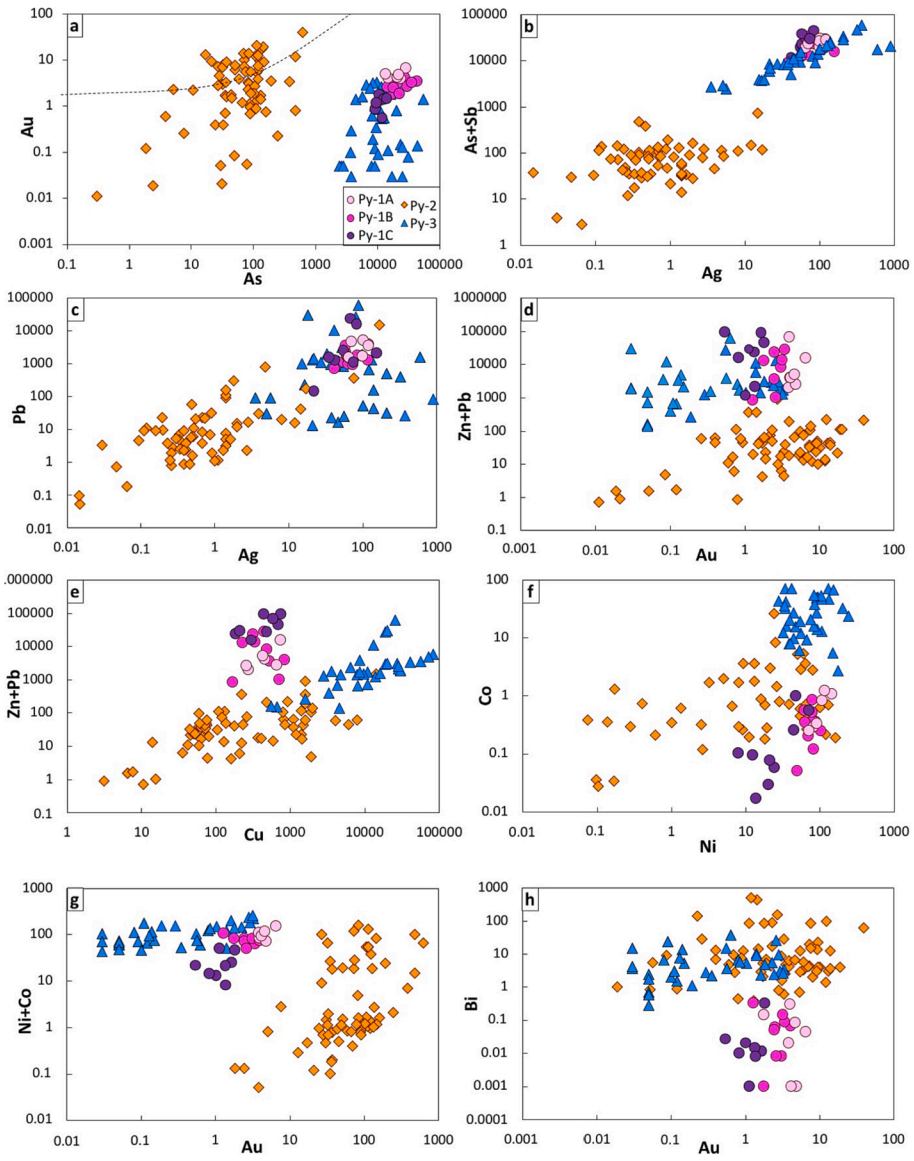

Fig. 8. Binary plots showing correlations of minor and trace elements detected by LA-ICP-MS from the different textural pyrite types selected for this study.

7. Discussion

7.1. An evaluation of the potential effects of deformation on pyrite

Empirical and experimental studies have shown that deformation of pyrite may operate along the brittle-ductile transition at <743 °C within the pressure interval of 1 to 3 kbar, with plastic deformation being active at temperatures potentially as low as ~200 °C (McClay and Ellis, 1983; Boyle et al., 1998; Freitag et al., 2004; Barrie et al., 2007; Barrie et al., 2009; Barrie et al., 2010). These P-T conditions overlap those of the peak of greenschists facies metamorphism (up to 300 °C at 2 kbar, Munhà, 1990; locally up to 3 kb, Marignac et al., 2003) that affected the IPB in the Hercynian orogeny. Deformation of pyrite within the ductile regime is recorded by plastic-like features such as internal lattice distortion, crystal bending, sub-grain formation or development of clustered CPO. In contrast, brittle deformation should produce cataclastic microstructures, grain size reduction and/or crack-seal (see Barrie et al., 2010).

The EBSD maps (BC and inverse pole) of the colloform polycrystalline aggregates of Py-1 are pristine as they do not reveal the presence of plastic or brittle deformational features (Fig. 3a-h). Further, these grains show cores (Py-1A) with dispersed CPO covered by layers of elongated-radiating (Py-1B) and faceted pyrite (Py-1C) with uniform CPO. These observations are inconsistent with deformational processes, as deformation should produce single CPO instead of abrupt changes as those observed between layers. Therefore, microstructures of Py-1 are considered here to be a primary precipitation feature unrelated to later deformation (Gao et al., 2016; Huang et al., 2020).

In contrast, Py-2 displays blocky subdomains (i.e., sub-grains) resembling the typical "mortar" microstructure of minerals that have experienced recovery after strain-related plastic deformation (e.g., Freitag et al., 2004). Empirical observations suggest that this mechanism of sub-grain recrystallization typically operates in pyrite at >400 °C and it is attributed to dislocation climb activated when it locks up as a result of an impediment during glide along a lattice plane (Barrie et al., 2010). In other words, pyrite embedded a higher refractive (highly-competent) matrix (e.g., quartz shown in Fig. 2d and f) behaves in a ductile manner. Once deformation ceased, pyrite may recover accumulating lattice distortion, which usually results in the formation of low-angle (≥2°) dislocation walls giving rise to sub-grain boundaries. The observation of sub-grain boundaries across spongy-looking cores and faceted rims may suggest full textural equilibrium as a result of recrystallization. It very likely reflects a re-arrangement of the internal microstructure during

recovery, consistently with the presence of single clusters of CPO in the inverse pole diagram (Fig. 3l; Barrie et al., 2009).

The uniformization of the CPO as a result of deformation is seemingly clearer in Py-3 than in Py-2, although sub-grain domains are observed in Py-2 alone (Fig. 3m-p). The absence of these internal plastic strain features in Py-3 may reflect the effect imposed by the relatively softer chalcopyrite matrix. It very likely acted as a cushion for accommodating the deformation thus enhancing pyrite grain growth without influence of the ambient deformation. Finally, brittle deformation is only preserved as a late crack seal in Py-3 (Fig. 3m-o) likely originated very late in the history of the deposits.

7.2. Formation and evolution of pyrite textures

The pristine microstructure of the colloform pyrite consists of an apparently conformable sequence of an earlier formed core (Py-1A) surrounded by two main concentric layers (Py-1B and Py-1C), indicating at least three main events of growth (Fig. 3a-h). These microstructural observations suggest growth of colloform polycrystalline aggregate from the core outward (Southam and Saunders, 2005; Falconer et al., 2006; Barrie et al., 2009; Gao et al., 2016; Huang et al., 2020).

The aggregates of finely-grained pyrite microcrystals (<5μm) with random orientation forming the cores of Py-1A were the seeds for the growth of acicular and elongated crystals of Py-1B. The specific alignment of the Py-1B acicular-elongated crystals reflects the geometrical effect of selection where only those growing perpendicularly to the substrate surface continued growing because it was energetically more favourable. Consistently, the band contrast EBSD maps reveal minute granular-like crystallites with random orientation at the bottom of discrete layers, thus suggesting that large elongated crystals with preferential CPO started to grow from this substrate (Fig. 3b-d and f-h). This also indicates a remarkable diversity in growth and nucleation rates within discrete layers and, potentially, in degree of supersaturation (e.g., Alonso-Azcárate et al., 2001). Such a case would support that discrete layers record pauses and resumption of growth in response to environmental changes. This is consistent with recent HRTEM observations showing no corrosion rinds and truncated nanoscale zoning within the inner portion of the colloform (contact Py-1A and Py-1B) and their existence in the outer portion of the colloform (contact Py-1B and Py1-C) (González-Jiménez et al., 2022).

Py-2 exhibits porous cores with several As-rich oscillatory zonation resembling those in Py-1 (Fig. 5b). These As-rich cores are traversed by subgrain boundaries (Fig. 3k), which suggests that overgrowth and aggregation of colloform material was prior to deformation, and very likely related to a late-stage temperature increase (Murowchick and Barnes, 1987; Sáez et al., 1999; Almodóvar et al., 2019). The occurrence of chalcopyrite and tetrahedrite inclusions in Py-2 (Fig. 2e, f, Fig. 4b and Fig. 5b) suggests that the textural shift from Py-1 to Py-2 was potentially controlled by hydrothermal fluids up to 350 °C, due to the dependence of the Cu solubility at high temperatures (Lydon, 1988; Almodóvar et al., 1998; Seward et al., 2014). Sulfides and sulfosalts now filling spaces suggest metal incorporation coevally or nearly after the pyrite aggregation, well before deformation induced recrystallization process of pyrite promoting development of faceted outlines.

Py-3 displays homogenous cores with no relict primary textures or subgrain boundaries (Fig. 3m-p), which suggests growth and/or recrystallization in a deformation-free environment influenced with progressively hotter fluids than typically operating in the VMS deposit. This is consistent with some massive sulfide deposits in the IPB (i.e., La Magdalena) recording a post-formation heating event due to intrusion of basic rocks previously to regional metamorphism (Almodóvar et al., 2019). The results of the experiments of Barrie et al. (2007) favour an increase in the temperature in the range 550–700 °C that enhanced recrystallization of pyrite by removing dislocations. These temperatures are slightly higher than temperatures estimated from: (1) fluid inclusions of many Cu-rich ores in the VMS deposits of the IPB (up to 400 °C; Sáez et al., 1999 and the references therein), and (2) mineral assemblages (tennantite, chalcopyrite, galena, gersdorffite and native gold) replacing Py-3 grain boundaries and/or filling late fractures and pores (Fig. 2i-l, Fig. 4b, Fig. 5c) (~350 °C; Lydon, 1988; Almodóvar et al., 1998; Seward et al., 2014; Revan et al., 2014; Grant et al., 2018). However, these temperatures are within the range of complete solidification of the intruding basic rocks, mainly gabbros, in the IPB (Contreras and Apalategui, 1999; Contreras et al., 1999), within the continental crust (~1000 °C).

7.3. Onset of the economic metal endowment in primary pyrites

Py-1 from Masa Valverde is richer in As, Zn, Pb and Sb than other primary pyrite from the IPB (Serrati et sl., 2002; Gaspar, 2002; Conde et al., 2020) but similar to pyrite from other VMS deposits elsewhere (Maslennikov et al., 2009; Genna and Gaboury, 2015; McClenaghan et al., 2004; Dehnavi et al., 2018; Grant et al., 2018). The Pb and Sb depletion from Py-1A to Py-1C (Fig. 7 and Appendix 3). reflects the presence or absence of inclusions of galena (<1 μm up to 25 μm; Fig. 2b-d) and tetrahedrite (<10 μm up to 50 μm; Fig. 2c-d), instead of their occurrence in solid solution within pyrite (Fig. 4band Fig. 5a). HRTEM observations by González-Jiménez et al. (2022) confirm that Pb is preferentially concentrated as scarce tiny (<50 nm) galena inclusions in the colloform and, to a lesser extent, as solid solution (preferentially in the outer portion), whereas Sb is systematically associated with nano-sized tetrahedrite particles that may or not be crystallographically related with the host pyrite. Positive correlations between Ag and Sb + As shown in Fig. 8b-c also suggests that Ag may come from tetrahedrite-tennantite inclusions in Py-1B and Py-1C as attested by Ag-As highs in time-resolved spectra collected by LA-ICP-MS (Fig. 6b) and HRTEM that confirm the presence of such particles at the nanoscale realm (see Fig. 4 in González-Jiménez et al., 2022). In contrast, the increase of Zn and Cu from Py-1A to Py-1C (Fig. 7 and Appendix 3) in absence of Zn- and Cu-bearing inclusions in Py-1C suggests that these elements were primarily fixed in the pyrite structure (Cook and Chryssoulis, 1990; Huston et al., 1995).

The textural relationship between Py-1A and very fine-grained galena (<1 μm) particles (Fig. 2b) suggests that galena crystallized prior or contemporarily to growing pyrite framboids (Huerta-Diaz and Morse, 1992; Morse and Luther, 1999; Koglin et al., 2010). However, progressively coarser galena particles towards the outer zones of Py-1 (Fig. 2a, c and d) raises the possibility that Pb-saturated fluids were still present during and after the formation of Py-1B and Py-1C. HRTEM investigations confirm the presence of these healed fractures even at the nanoscale with droplet-like galena particles attached to pores corresponding to former fluid inclusions connected to these nano-sized fractures (González-Jiménez et al., 2022). Interestingly, Py-1 records a negative correlation between Fe and As in a trend approximately parallel to the Fe–As join in As-Fe-S ternary diagram (Fig. 9). Such chemical trends are interpreted to reflect As^{3+} by Fe^{2+} substitution in pyrite under slightly oxic environments (Chouninard et al., 2005; Morey et al., 2008; Deditius et al., 2008; Deditius et al., 2009a; Deditius et al., 2009b), consistently with previous works describing nearly oxic conditions at the earliest stages of VMS mineralization along the IBP (Fig. 10; Almodóvar et al., 1998; Inverno et al., 2008; Sáez at al., 2011). In the Masa Valverde and La Magdalena deposits, nearly oxic conditions are marked by the precipitation of early magnetite and/or barite (Almodóvar et al., 2019). Both magnetite and/or barite have been linked to precipitation processes from HS^--poor and slightly oxidized hydrothermal fluids (Ohmoto, 1996), as also identified in other VMS deposits (e.g., Kuroko, Japan; Ohmoto, 1996).

Under such redox conditions, the structure of Py-1A may also host some Ag^+ and Sb^{3+} through Fe^{2+} substitution (Chouninard et al., 2005; Deditius et al., 2014). This could explain why Py-1A and certain inner domains of Py-1B do not contain visible inclusions of Ag and Sb. In contrast, Py-1B shows also a second trend parallel to the As–S join

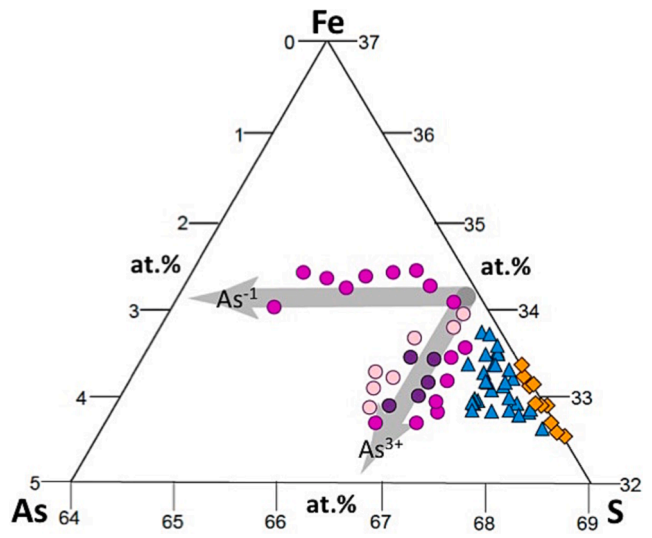

Fig. 9. Ternary Fe–S–As (at.%) diagram comparing the EPMA composition of different textural pyrite types. Py-1 (pink circles) shows two different trends suggesting substitution of both As for S and As for Fe. Dispersed analyses of Py-2 (blue triangles) and Py-3 (orange diamonds) suggests the presence of nanoparticles and/or additional trace elements bounded in lattice as well as probable vacancies in the Fe and S sites (Deditius et al., 2008). (For interpretation of the references to color in this figure legend, the reader is referred to the web version of this article.)

suggesting also the S^{-1} by As^{-1} substitution (Fig. 9), which is common under reducing conditions (Fleet and Munin, 1997; Simon et al., 1999; Savage et al., 2000; Pals et al., 2003; Zachariáš et al., 2004; Reich et al., 2005; Blanchard et al., 2007; Liang et al., 2013). This bimodal substitution of As in Py-1B, together with the tiny arsenopyrite particles (<0.5 μm) parallel to the colloform layers (Fig. 2c and Fig. 5a), may explain its singular enrichment in As (Fig. 7 and Appendix 3). Successive pulses of physico-chemically variable hydrothermal fluids shifted the elemental partitioning in pyrite, where galena and tetrahedrite sequestered most of the Pb, Sb and Ag as observed within Py-1B and Py-1C (Fig. 2a, c and d), and Zn and Cu were mainly hosted in Py-1C (Fig. 6 and Appendix 3). The occurrence of some of these metals in Py-1 (Fig. 6a) suggests that this pyrite type exsolved some particles contemporarily to dissolution-reprecipitation during pause and resumption of pyrite growth (e.g., Deditius et al., 2011). This is consistent with nanoscale observation of tetrahedrite particles with identical crystallographic orientation to pyrite matrices colloform aggregated (see Fig. 7d in González-Jiménez et al, 2022). Interestingly, the formation of mineral inclusions coincides with the onset of the economic metal endowment in polymetallic mineralization in the IPB.

Au shows positive correlation with As in Py-1 and plots below the Au solubility limit defined by Reich et al. (2005) (Fig. 8a), thus suggesting that Au occurs dominantly as a structurally bound element. This is also supported by the lack of native gold particles visible at SEM and HRTEM scales as well as LA-ICP-MS profiles (Fig. 6a and b). The incorporation of Au in pyrite is thought to occur as a result of the substitution of Au^{1+} for Fe^{2+} (e.g., Trigub et al., 2017; Merkulova et al., 2019; Filimonova et al., 2020) and to be favoured by structural distortion or superficial effects caused by the incorporation of cationic or anionic As (Simon et al., 1999; Palenik et al., 2004; Deditius et al., 2008; Deditius et al., 2014). The Au depletion from Py-1A to Py-1C (Fig. 7 and Appendix 2) may be explained by changes in the Au and As contents of ore-forming fluids (Fougerouse et al., 2016).

7.4. Critical metal mobility during local leaching and Variscan deformation

Slightly higher As contents in the cores relative to the rims of Py-2 are observed in the form of sector zoning. Such feature is apparently unrelated with mineral inclusions (Fig. 5b, Fig. 6c and d) and interpreted as inherited from the earlier-formed precursor Py-1 (Fig. 2a and Fig. 5a), thus denning exsolution-related processes suggested in other instances for pyrite affected by thermal overprint (Kusebauch et al., 2018). In contrast, the rims of Py-2 contain several particles of tetrahedrite and arsenopyrite imaged by both FESEM (Fig. 2f and Fig. 5b) and LA-ICPMS profiles (Fig. 6c and d). It led us to suggest that As and other metals such as Sb, Cu, Ag were primarily fixed by these minerals at the reaction front between pre-existing Py-1 and later ore-forming fluids. This could reflect processes of coupled dissolution-reprecipitation (e.g., Putnis, 2002; Putnis, 2009) that removed certain amounts of metals originally present in the pyrite at lattice level or as (in)visible particles (e.g., Chouinard et al., 2005; Deditius et al., 2008; Barker et al., 2009; Large et al., 2009) and/or supplied by the incoming fluid. These As-rich rims are also crosscut by sub-grain boundaries (Fig. 3k), suggesting that these minerals and their host faceted rims formed before the deformational event. It very likely took place soon after As-rich cores coalesced as a result of later fluids towards waning of the VMS related phenomena.

Characteristically, Py-2 is rich in Bi (up to 520 ppm) and Au (up to 39 ppm), and into a lesser extent in Co and Ni (Fig. 7; Appendix 3). Such endowment in (semi)-metals is decoupled from As (Fig. 5b), suggesting that these elements entered in the pyrite the structure unrelated with As, unlike hydrothermal pyrite elsewhere (Reich et al., 2006; Reich et al., 2011; Mikhlin et al., 2011; Deditius et al., 2011; Hough et al., 2011). The random distribution of Au particles in Py-2 (Fig. 2e, Fig. 4j and Fig. 5b) also suggests a more complex origin than previously reported for hydrothermal pyrite in other deposits (Leistel et al., 1998; McClenaghan et al., 2004; McClenaghan et al., 2009; Wright et al., 2016; Reich et al., 2005). The largest native gold particles in Py-2 pores (Fig. 2e) and within chalcopyrite (Fig. 2g) are the most likely candidates for direct precipitation from Au-saturated mineralizing fluids (Yang et al.,1998). In contrast, native gold particles detected by means of LA-ICP-MS (Fig. 6d) in apparently inclusion-free zones under FE-SEM (Fig. 2f) may be attributed to solid-state remobilization of Au originally hosted in pyrite coarsened by later invigorating ore system (Reich et al., 2006) during the latest stages of VMS mineralization. Alternatively, it could be related to later hydrothermal events associated with emplacement of mafic rocks in the footwall of the deposit previously to deformation on the Hercynian times. This seems to be consistent with the coeval enrichment of Au and Co + Ni apparently fingerprinting the entrance of relative hot fluids associated to these mafic rocks (see next section).

It is worth to note that the proposed mechanism has already been invoked to explain other trace metal-poor pyrites in hydrothermal deposits elsewhere (e.g., Hannington et al., 1998a; Yuan et al., 2018). These latter authors proposed that pyrite that has experienced multiple episodes of refining and recrystallization may become depleted in (semi)-metals such Cu, Mn, Zn, Cd, Pb, Ag, and Ga, which were reincorporated into sulfides in other areas of the deposit. In fact, our Py-2 shows remarkable overall low concentrations and abundance of mineral inclusions of As, Sb, Ag, Zn, Pb and Cu than Py-1 and Py-3, indeed reflecting that late fluids additionally removed these(semi)-metal. Nevertheless, the presence of relicts of chalcopyrite, galena and tennantite encapsulated in Py-2 (Fig. 2e and f) suggests that this process was incomplete in the studied deposits.

On the other hand, Sb and Bi, and to a lesser extent Zn and Ag, are anomalously enriched in the sub-grain domain boundaries of Py-2 (Fig. 3k and Fig. 5b). This suggests that some quantities of these (semi)-metals were mobilized either coevally or after deformation-related recrystallization of pyrite (Fig. 10). Regional low-grade metamorphism in the IPB (Silva et al., 1990) attained peaks up to 300 °C at 2 kb (Munhá, 1990), thus overlapping the temperature range proposed for

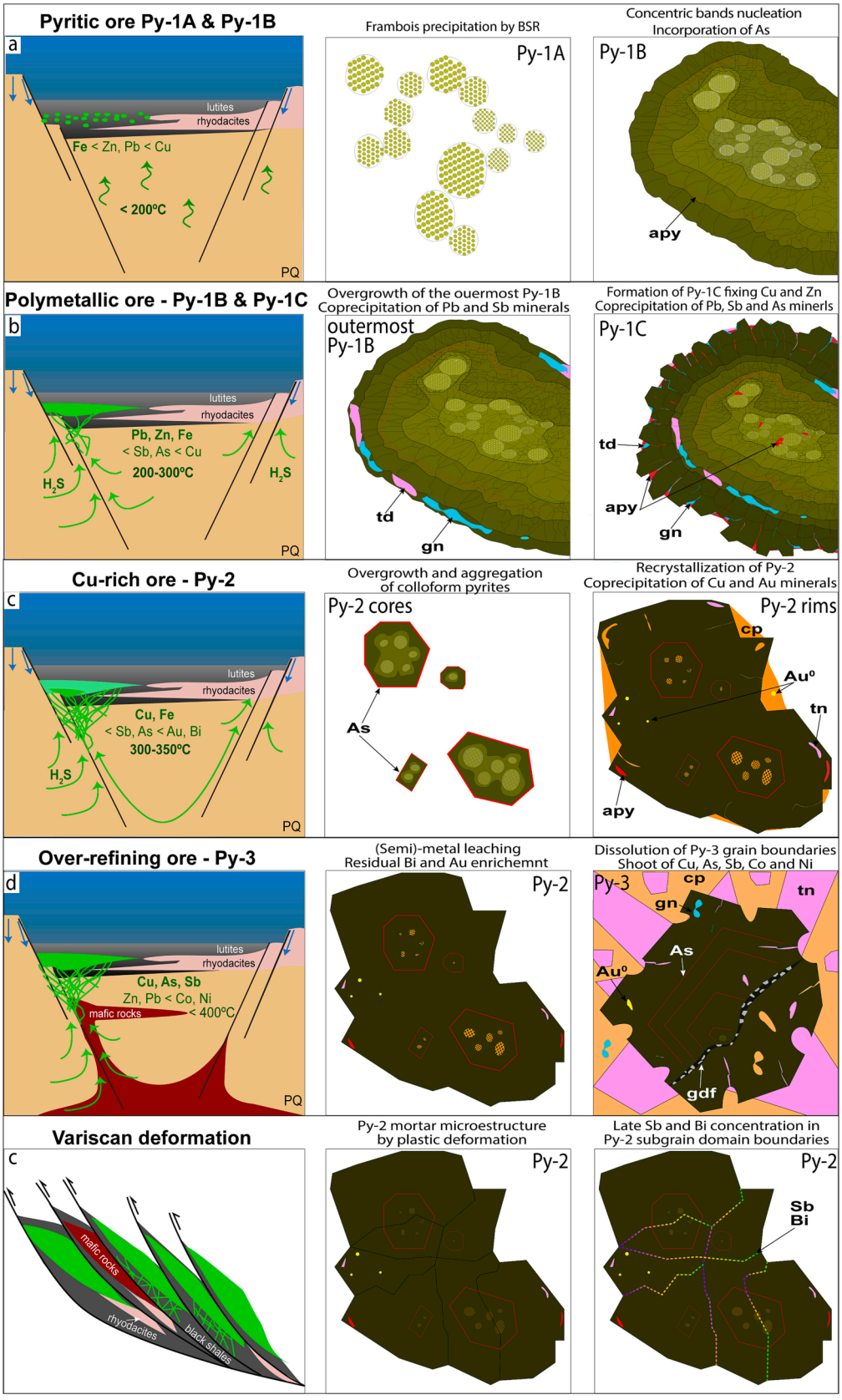

Fig. 10. Summary schematic of trace elements linked to textural evolution in pyrites from VMS deposits of the IPB. Low-temperature fluid flow led to the precipitation of primary pyrite textures (Py-1A and Py-1B) (a). The onset of the economic metal endowment in pyrites began with the recrystallization of primary pyrite (Py-1c) together with the coprecipitation of polymetallic ores (b), followed by the formation of the Cu-rich ore at increasing temperatures (c). Over-refining processes associated with the late emplacement of mafic rocks at the footwall of the deposits resulted in both leached pyrites (Py-2C) and high grades ores (Py-3) (d) Hercynian deformation involved Py-2 plastic deformation and concentration of (semi)-metals in the subgrain domain boundaries. Keys: apy = arsenopyrite; td = tetrahedrite; gn = galena; cp = chalcopyrite; tn = tennantite; gdf = gersdorffite.

metal releasing from pyrite via solid-state diffusion during metamorphism (e.g., Huston et al., 1995; Tomkins et al., 2007). Our analytical approach to sub-grain boundaries (Fig. 5b and Fig. 6d) matched clusters of Sb, Bi, Zn and Ag concentrated by diffusion processes and associated with pyrite dislocation in the sub-grain boundaries of Py-2 (Fougerouse et al., 2021). Alternatively, fluids carrying these elements would have circulated across the already formed sub-grain boundaries and precipitated nano-sized clusters of native Sb and Bi or Bi-Sb sulfosalts, as previously reported in other deposits of the IPB (García de Miguel,1990; Gaspar, 2002; Yesares et al., 2015; Almodóvar et al., 2019). Fluids associated to late post-Hercynian reactivation of the hydrothermal systems, and the extensional rejuvenation of pre-existing fractures, responsible of Sb vein-type mineralizations in the area (Germann et al., 2003).

7.5. Critical metal enrichment by over-refining processes

Py-3 displays As-rich zoned cores with a faceted morphology similar to those documented for Py-2 (Fig. 2j, Fig. 4c, Fig. 5c). Such relict features confirm that these Py-2 and Py-3 had a common Py-1 precursor, which underwent structural and chemical modification during waning stages of VMS. However, Py-3 does not record the latest event of deformation documented in Py-2 owing to its embedding in a softer chalcopyrite matrix. Interestingly, Py-3 is notably enriched in most of the analyzed minor and trace elements (Cu, Ag, Ni, Co, As, Zn, Sb, Pb) (Fig. 7 and Appendix 3). As noted above, the homogenous internal structure of Py-3 (Fig. 3m) was produced by a thermal overprint that was most likely induced by the hot emplacement of basic rocks. High grade ores are well known in VMS deposits and commonly interpreted as the result of late over-refining processes linked to thermal overprint (Eldridge and Barton, 1983; Hannington et al., 1998a; Petersen et al., 2000; Yuan et al., 2018). In the IPB, the origin of high-grade mineralization in the VMS deposits has been previously related to a "mafic" contributor (e.g., Almodóvar et al., 2019).

Previous works have shown that Co and Ni contents in hydrothermal pyrite may fingerprint the contribution of (ultra)-mafic rocks/magmas to the metal tenor of magmatic-hydrothermal deposits (Thompson et al., 2001; Hanley and MacKenzie, 2009; Hanley et al., 2010; González-Jiménez et al., 2021), for Ni and Co are akin to ultramafic and mafic magmas but depleted in felsic rocks (Zierenberg et al., 1993; Hattori et al., 2002). The scarcity of Co and Ni in Py-1 from Masa Valverde is consistent with the felsic character of volcanoclastic hosting rocks (Ruiz et al., 2002). In contrast, the high concentration of Co and Ni in Py-2, and above all, in Py-3 (Fig. 7 and Appendix 3) from la Magdalena deposit match a possible elemental input of the intrusive basic rocks. These two metals could enter in the pyrite as stoichiometric substitutions, such as Co^{2+} and Ni^{2+} for Fe^{2+} (Vaughan and Craig, 1978; Tossell et al., 1981; Abraitis et al., 2004; Gregory et al., 2015). Such contribution of the basic rocks is not only recorded in pyrite itself but also by the presence of Co-sulfosalts (e.g., gersdorsffite) filling late micro-fractures in Py-3 (Fig. 2l, Fig. 6e and f). These observations all together seem to suggest that Ni and Co could be scavenged by hydrothermal fluids under moderately to strongly reduced conditions from the spatially associated intruding rocks (e.g., Yamamoto et al., 1984; Auclair et al., 1987; Huston et al., 1995; Hannington et al., 1999a; Hannington et al., 1999b; Maslennikov et al., 2009, 2017; Revan et al., 2014; Genna and Gaboury, 2015; Keith et al., 2016).

In the proposed model, the mafic sills could act as both thermic engine that reactivated the hydrothermal system and as a source themselves of metals which could be mobilized by the hydrothermal fluids (Fig. 10). In this geological framework, ores closer to the intrusion should have interacted with these late hydrothermal fluids becoming depleted in most (semi)-metals, thus giving rise to Py-2. Then, the hydrothermal fluids loaded in these leached metals migrated towards other zones of the deposit originating the Py-3 ore enriched in those (semi)-metals leached from Py-2.

8. Conclusions

The sequence of pyrite textural maturation in VMS deposits from the IPB are well preserved and distinguishable under optical reflected and electronic microscopy. EBSD reveals that framboidal, colloform and recrystallized pyrite textures formed locally at increasing temperatures and locally also by deformation related with regional metamorphic overprint. VMS deposits of the IPB record a complex geochemical and mineralogical evolution of pyrite that is consistent with the following hydrothermal ore-forming processes: (1) precipitation of primary pyrite (Py-1) during the earliest stages of formation of massive sulfide lenses that resulted in core-to-rim impoverishment in certain metals such as Pb, Sb, Ag and Au, linked to the formation of progressively coarser galena and tetrahedrite, and an increase in Zn and Cu contents in the pyrite lattice; (2) Pyrite depleted in (semi-) metals (Py-2) associated with enriched pyrite (Py-3), thus suggesting transference of metals from leached zones to high-grade ores; and (3) pyrite associated with over-refining areas (Py-2 and 3) showing a general enrichment in Co and Ni, which may record an overprinting thermal event likely related to the emplacement of mafic rocks in the footwall of the deposits.

Declaration of Competing Interest

The authors declare that they have no known competing financial interests or personal relationships that could have appeared to influence the work reported in this paper.

Data availability

No data was used for the research described in the article.

Acknowledgements

This research is a contribution to the projects CGL2016-79204-R, PID2019-111715GB-I00 which are supported by the Spanish Government, and 18/IF/6347 granted by Science Foundation Ireland (SFI). The authors thank Cambridge Minerals for access to drill core, sampling assistance and the ongoing collaboration. We are also grateful to Teodosio Donaire for his constructive suggestions in petrogenetic aspects of volcanogenic rocks in the IPB as well as Dany Savard and Audrey Lavoie of LabMaTer, UQAC, for their assistance during the laser ablation analyses. Authors would also like to acknowledge the use of Servicio General de Apoyo a la Investigación-SAI, Universidad de Zaragoza.

Appendix. Supplementary material

Supplementary data to this article can be found online at https://doi.org/10.1016/j.oregeorev.2022.105275.

References

Abraitis, P.K., Pattrick, R.A.D., Vaughan, D.J., 2004. Variations in the compositional and electrical properties of natural pyrite: a review. International Journal Mineral Processing 74, 41–59.

Almodóvar, G.R., Sáez, R., Pons, J.M., Maestre, A., Toscano, M., Pascual, E., 1998. Geology and genesis of the Aznalcóllar massive sulphide deposits. Iberian Pyrite Belt, Spain: Mineralium Deposita 33, 111–136.

Almodóvar, G.R., Yesares, L., Sáez, R., Toscano, M., González, F., Pons, J.M., 2019. Massive sulfide ores in the Iberian Pyrite Belt: mineralogical and textural evolution. Minerals 9, 653.

Alonso-Azcárate, J., Rodas, M., Fernández-Díaz, L., Bottrell, S., Mas, J.R., López-Andrés, S., 2001. Causes of variation in crystal morphology in metamorphogenic pyrite deposits of the Cameros Basin (N Spain). Geological Journal 36, 159–170.

Auclair, G., Fouquet, Y., Bohn, M., 1987. Distribution of selenium in high-temperature hydrothermal sulfide deposits at 13 degrees North. East Pacific Rise: Canadian Mineralogist 24, 577–587.

Barker, S., Hickey, K.A., Cline, J.S., Dipple, G.M., Kilburn, M., Vaughan, J.R., Longo, A. A., 2009. Uncloaking invisible gold: use of nanosims to evaluate gold, trace elements, and sulfur isotopes in pyrite from Carlin-type gold deposits. Economic Geology 104, 897–904.

Barrie, C.D., Boyce, A.J., Boyle, A.P., Williams, P.J., Blake, K., Ogawara, T., Akai, J., Prior, D.J., 2009. Growth controls in colloform pyrite. American Mineralogist 94, 415–429.
Barrie, C.D., Boyle, A., Cook, N.J., Prior, D., 2010. Pyrite deformation textures in the massive sulfide ore deposits of the Norwegian Caledonides. Tectonophysics 483, 269–286.
Barrie, C.D., Boyle, A.P., Prior, D.J., 2007, An analysis of the microstructures developed in experimentally deformed polycrystalline pyrite and minor sulphide phases using electron backscatter diffraction: Journal of Structural Geology, v. 29 (9), p. 1494–1511.
Blanchard, M., Wright, K., Catlow, R.A., 2007. Arsenic incorporation into FeS_2 pyrite and its influence on dissolution: a DFT study. Geochimica et Cosmochimica Acta 71, 624–630.
Boyle, A.P., Prior, D.J., Banham, M.H., Timms, N.E., 1998. Plastic deformation of metamorphic pyrite: new evidence from electron-backscatter diffraction and forescatter orientation-contrast imaging. Mineralium Deposita v. 34 (1), 71–81.
Carvalho, D., 1976. Considerações sobre o vulcanismo de Cercal-Odemira, sues relações com a Faixa Piritosa. Comunicações Serviços Geológicos Portugal 60, 215–238.
Castroviejo, R., Quesada, C., 2011. Soler, M, Post-depositional tectonic modification of VMS deposits in Iberia and its economic significance. Mineralium Deposita 46, 615–1537.
Chouninard, A., Paquete, J., William-Jones, E., 2005. Crystallographic control son trace-elenent incorporation in auriferous pyrite from the pascua epithermal high-sulfidation deposit, Chile-Argentina. Canadian Mineralogist 43, 951–953.
European Commision, 2020, Study on the EU's list of Critical Raw Materials (https://rmis.jrc.ec.europa.eu/?page=crm-list-2020-e294f6).
Conde, C., Tornos, F., Danyushevsky, L.V., Large, R., 2020. Laser ablation-ICPMS analysis of trace elements in pyrite from the Tharsis massive sulphide deposit, Iberian Pyrite Belt (Spain). Journal of Iberian Geology 47, 429–440.
Contreras, F., Apalategui, 1999, Mapa Geológico a escala 1:50.000 y Memoria de Puebla de Guzmán (958). Investigación Geológica y Cartografía Básica en la Faja Pirítica y Áreas Aledañas (www.juntadeandalucia.es/innovacioncienciayempresa/sigma/index.html).
Cook, N.J., Chryssoulis, S.L., 1990. Concentrations of "invisible gold" in the common sulfides. Canadian Mineralogist 28, 1–16.
Deditius, A.P., Utsunomiya, S., Renock, D., Ewing, R.C., Ramana, C.V., Becker, U., Kesler, S.E., 2008. A proposed new type of arsenian pyrite: composition, nanostructure and geological significance. Geochimica et Cosmochimica Acta 72, 2919–2933.
Deditius, A.P., Utsunomiya, S., Ewing, R.C., Kesler, S.E., 2009a. Nanoscale "liquid" inclusions of As–Fe–S in arsenian pyrite. American Mineralogist 94, 391–394.
Deditius, A.P., Utsunomiya, S., Ewin, R.C., Chryssoulis, S.L., Venter, D., Kesler, S.E., 2009b. Decoupled geochemical behaviour of As and Cu in hydrothermal systems. Geology 37, 707–710.
Deditius, A.P., Reich, M., Kesler, S.E., Utsunomiya, S., Chryssoulis, S.L., Walshe, J., Ewing, R.C., 2014. The coupled geochemistry of Au and As in pyrite from hydrothermal ore deposits. Geochimica et Cosmochimica Acta 140, 644–670.
Deditius, A., Utsunomiya, S., Reich, M., Kesler, S.E., Ewing, R.C., Hough, R., Walshe, J., 2011. Trace metal nanoparticles in pyrite. Ore Geology Reviews 42, 32–46.
Dehnavi, A.S., McFarlane, C.R.M., Lents, D.R., Walker, J.A., 2018. Assessment of pyrite composition by LA-ICP-MS techniques from massive sulfide deposits of the Bathurst Mining Camp, Canada: From textural and chemical evolution to its application as a vectoring tool for the exploration of VMS deposits. Ore Geology Reviews 92, 656–671.
Eldridge, C.S., Barton, P.B., 1983. Ohmoto, H, Mineral textures and their bearing on formation of the Kuroko orebodies. Economic Geology Monographs 5, 241–281.
Falconer, D.M., Craw, D., Youngson, J.H., Faure, K., 2006. Gold and sulphide minerals in tertiary quartz pebble conglomerate gold placers. Southland, New Zealand: Ore Geology Reviews 28, 525–545.
Filimonova, O.N., Tagirov, B.R., Trigub, A.L., Nickolsky, M.S., Rovezzi, M., Belogub, E. V., Maximilian, S., Reukov, V.L., Vikentyev, V., 2020. The state of Au and As in pyrite studied by X-ray absorption spectroscopy of natural minerals and synthetic phases. Ore Geology Reviews 121, 103475.
Fleet, M.E., Munin, H., 1997. Gold-bearing arsenian pyrite and marcasite and arsenopyrite from Carlin Trend gold deposits and laboratory synthesis. American Mineralogist 82, 182–193.
Fougerouse, D., Mickletwaite, S., Tomkins, A.G., Mei, Y., Kilburn, M., Guadliardo, P., Fisher, L.A., Halfpenny, A., Gee, M., Paterson, D., Howard, D.L., 2016. Gold remobilization and formation of high-grade ore shoots driven by dissolution-reprecipitation replacement and Ni substitution into auriferous arsenopyrite. Geochimica et Cosmochimica Acta 178, 143–159.
Fougerouse, D., Reddy, S.M., Aylmore, M., Yang, L., Guagliardo, P., Saxey, D.W., Rickard, W.D.A., Timms, N., 2021. A new kind of invisible gold in pyrite hosted in deformation-related dislocations. Geology v. 49 (10), 1225–1229.
Franklin, J.M., Sangster, D.M., Lydon, J.W., 1981, Volcanic-associated massive sulfide deposits: Economic Geology, v. 75th Anniversary, p. 485–627.
Franklin, J.M., Gibson, H.L., Jonasson, I.R., Galley, A.G., Hedenquist, J.W., Thompson, J. F.H., Goldfarb, R.J., Richards, J.P., 2005, Volcanogenic Massive Sulfide Deposits: Society of Economic Geologists, v. 100th Anniversary, p. 525-560.
Freitag, K., Boyle, A.P., Nelson, E., Hitzman, M., Churchill, J., Lopez-Pedrosa, M., 2004. The use of electron backscatter diffraction and orientation contrast imaging as tools for sulphide textural studies: example from the Greens Creek deposit (Alaska). Mineralium Deposita v. 39 (1), 103–113.
Galley, A.G., Hannington, M.D., Jonasson, I.R., 2007, Volcanogenic massive sulfide deposits, in Goodfellow, W.D., ed., Mineral deposits of Canada: a synthesis of major deposit types, district metallogeny, the evolution of geological provinces, and exploration methods:. Geological Association Canada, Special Publication 5, Mineral Deposits Division, p. 141–161.
Gao, S., Huang, F., Gu, X., Chen, Z., Xing, M., Li, Y., 2016. Research on the growth orientation of pyrite grains in the colloform textures in Baiyunpu Pb–Zn polymetallic deposit. Hunan, China: Mineralogy and Petrology 111, 69–79.
García de Miguel, J.M., 1990. Mineralogía, paragénesis y sucesión de los sulfuros masivos en la Faja Pirítica en el suroeste de la Península Ibérica. Boletín Geológico y Minero 101, 73–105.
Gaspar, O.C., 2002. Mineralogy and sulfide mineral chemistry of the Neves-Corvo ores, Portugal: insight into their genesis. Canadian Mineralogist 40, 611–636.
Genna, D., Gaboury, D., 2015. Deciphering the hydrothermal evolution of a VMS system by LA-ICP-MS using trace elements in pyrite: An example from the Bracemac-McLeod deposits. Abitibi, Canada, and implications for exploration: Economic Geology 110, 2087–2108.
U.S. Geological Survey, 2022, Mineral Commodity Summaries (https://doi.org/10.3133/mcs2022).
Germann, K., Lüders, V., Banks, D.A., Simon, K., Hoefs, J., 2003. Late Hercynian polymetallic vein-type base-metal mineralization in the Iberian Pyrite Belt: fluid-inclusion and stable-isotope geochemistry (S–O–H–Cl). Mineralium Deposita 38, 953–967.
González-Jiménez, J.M., Piña, R., Kerestedjian, T.N., Gervilla, F., Borrajo, I., Farré-de-Pablo, J., Proenza, J.A., Tornos, F., Roqué, J., Nieto, F., 2021. Mechanisms for Pd-Au enrichment in porphyry-epithermal ores of the Elatsite deposit, Bulgaria. Journal of Geochemical Exploration 220, 106664.
González-Jiménez, J.M., Yesares, L., Piña, R., Sáez, R., Almodóvar, G.R., Nieto, F., Tenorio, S., 2022. Polymetallic nanoparticles in pyrite from VMS deposits of the Iberian Pyrite Belt. Ore Geology Reviews 145, 104875.
Granda-Sanz, A., Granda-Paris, T., Pons, J.M., Videira, J.C., 2019. El descubrimiento del Yacimiento de la Magdalena. Protagonismo de los métodos geofísicos en la exploración de yacimientos tipo sulfuros masivos vulcanogénicos (VMS) profundos en la faja pirítica ibérica. Boletín Geológico y Minero v. 130 (2), 213–230.
Grant, H.L.J., Hannington, M.D., Petersen, S., Frische, M., Fuchs, S.H., 2018. Constraints on the behavior of trace elements in the actively forming TAG deposit. Mid-Atlantic Ridge, based on LA-ICP-MS analyses of pyrite: Chemical Geology 498, 45–71.
Gregory, D.D., Large, R.R., Halpin, J.A., Baturina, E.L., Lyons, T.W., Wu, S., Danyushevsky, L., Sack, P.J., Chappaz, A., Maslennikov, V.V., Bull, S.W., 2015. Trace element content of sedimentary pyrite in black shales. Economic Geology 110, 1389–1410.
Hanley, J.J., MacKenzie, M., 2009. Incorporation of platinum-group elements and cobalt into subsidiary pyrite in alkalic Cu-Au porphyry deposits: significant implications for precious metal distribution in felsic magmatic-hydrothermal systems: AGU Spring Meeting. Abstract 2009, V14A–V.
Hanley, J.J., MacKenzie, M.K., Warren, M.R., Guillong, M., 2010. Distribution and origin of platinum-group elements in alkalic porphyry Cu–Au and low sulfidation epithermal Au deposits in the Canadian Cordillera: 11th International Platinum Symposium. Extended Abstract 21–24.
Hannington, M.D., Jonasson, I.R., Herzig, P.M., Petersen, S., 1995. Physical and chemical processes of seafloor mineralization at midocean ridges. In: Humphris, S.E., Zierenberg, R.A., Mullineaux, L.S., Thomson, R.E. (Eds.), Seafloor Hydrothermal Systems: Physical, Chemical, Biological and Geological Interactions: Geophysical Monograph 91. American Geophysical Union, pp. 115–157.
Hannington, M.D., Barrie, C.T., Bleeker, W., 1999a. The Giant Kidd Creek Volcanogenic Massive Sulfide Deposit, Western Abitibi Subprovince. Canada; summary and synthesis: Economic Geological Monographs 10, 661–672.
Hannington, M.D., Poulsen, K.H., Thompson, J.F.H., Sillitoe, R.H., 1999b. Volcanogenic gold in the massive sulfide environment: Review. Economic Geology 8, 325–356.
Hannington, M.D., 2014, 13.18 - Volcanogenic Massive Sulfide Deposits, in Holland, H. D., and Turekian, K.K., eds., Treatise on Geochemistry (Second Edition): Elsevier, Oxford, p. 463-488.
Hough, R.M., Noble, R.R.P., Reich, M., 2011. Natural gold nanoparticles. Ore Geology Reviews 42, 55–61.
Huang, F., Gao, S., Chen, L., Su, L., Li, Y., Meng, L., Liu, K., Chai, C., Qi, X., 2020. Micro-texture and in situ sulfur isotope of pyrite from the Baiyunpu Pb–Zn deposit in central Hunan, South China: Implications for the growth mechanism of colloform pyrite aggregates: Journal of Asian. Earth Science 193, 104302.
Huerta-Diaz, M.A., Morse, J.W., 1992. Pyritization of trace metals in anoxic marine sediments. Geochimica et Cosmochimica Acta 56, 2681–2702.
Huston, D.L., Sie, S.H., Suter, G.F., Cooke, D.R., Both, R.A., 1995, Trace elements in sulfide minerals from eastern Australian volcanic-hosted massive sulfide deposits: Part I, Proton microprobe analyses of pyrite, chalcopyrite, and sphalerite, and Part II. Selenium levels in pyrite; comparison with δ34S values and implications for the source of sulfur in volcanogenic hydrothermal systems: Economic Geology, v. 90, p. 1167-1196.
Huston, D.L., Large, R.R., 1989. A chemical model for the concentration of gold in volcanogenic massive sulphide deposits. Ore Geology Reviews 4, 171–200.
Inverno, C.M.C., Solomon, M., Barton, M.D., Foden, J., 2008. The Cu stockwork and massive sulfide ore of the Feitais volcanic-hosted massive sulfide deposit, Aljustrel, Iberian Pyrite Belt, Portugal: a mineralogical, fluid inclusion, and isotopic investigation. Economic Geology 103, 241–267.
Keith, M., Häckel, F., Haase, K.M., Schwarz-Schampera, U., Klemd, R., 2016. Trace element systematics of pyrite from submarine hydrothermal vents. Ore Geology Review 72, 728–745.
Koglin, N., Frimmel, H.E., Minter, W.E.L., Brätz, H., 2010. Trace-element characteristics of different pyrite types in Mesoarchaean to Palaeoproterozoic placer deposits. Mineralium Deposita 45, 259–280.

Large, R.R., 1992. Australian volcanic-hosted massive sulfide deposits; features, styles, and genetic models. Economic Geology 8, 471–510.
Large, R., Danyushevsky, L., Hollit, C., Maslennikov, V., Meffre, S., Gilbert, S., Bull, S., Scott, R., Emsbo, P., Thomas, H., 2009. Gold and trace element zonation in pyrite using a laser imaging technique: Implications for the timing of gold in orogenic and Carlin-style sediment-hosted deposits. Economic Geology 104, 635–668.
Layton-Matthews, D., Peter, J.M., Scott, S.D., Leybourne, M.I., 2008. Distribution, Mineralogy, and Geochemistry of Selenium in Felsic Volcanic-Hosted Massive Sulfide Deposits of the Finlayson Lake District, Yukon Territory, Canada. Economic Geology 103, 61–88.
Liang, J.L., Sun, W.D., Li, Y.L., Zhu, S.Y., Li, H., Liu, Y.L., Zhai, W., 2013. An XPS study on the valence states of arsenic in arsenian pyrite: implications for Au deposition mechanism of the Yang-shan Carlin-type gold deposit, western Qinling belt. Journal of Asian Earth Sciences 62, 363–372.
Lydon, J.W., 1988. Ore Deposit Models #14. Volcanogenic Massive Sulphide Deposits Part 2: Genetic Models. Geoscience Canada v. 15 (1), 43–65.
Makvandi, S., Ghasemzadeh-Barvarz, M., Beaudoin, G., Grunsky, E.C., McClenaghan, M. B., Duchesne, C., Boutroy, E., 2016. Partial least squares-discriminant analysis of trace element compositions of magnetite from various VMS deposit subtypes: Application to mineral exploration. Ore Geology Reviews 78, 388–408.
Marcoux, E., Moëlo, Y., Leistel, J.M., 1996. Bismuth and cobalt minerals: indicators of stringer zones to massive sulfide deposits. Iberian Pyrite Belt: Mineralium Deposita 31, 1–26.
Marignac, C., Diagana, B., Cathelineau, M., Boiron, M.C., Banks, D., Fourcade, S., Jean Vallance, J., 2003. Remobilisation of base metals and gold by Variscan metamorphic fluids in the south Iberian pyrite belt: evidence from the Tharsis VMS deposit. Chemical Geology 194, 143–165.
Maslennikov, V., Maslennikova, S., Large, R., Danyushevsky, L., 2009. Study of trace element zonation in vent chimneys from the Silurian Yaman-Kasy volcanic-hosted massive sulfide deposit (southern Urals, Russia) using laser ablation-inductively coupled plasma mass spectrometry (LA-ICPMS). Economic Geology 104, 1111–1141.
Maslennikov, V.V., Maslennikova, S.P., Large, R.R., Danyushevsky, L.V., Herrington, R. J., Ayupova, N.R., Zaykov, V.V., Lein, Y.A., Tseluyko, A.S., Melekestseva, Y.u., I., Tessalina, S.G., 2017. Chimneys in Paleozoic massive sulfide mounds of the Urals VMS deposits: Mineral and trace element comparison with modern black, grey, white and clear smokers. Ore Geology Reviews 85, 64–106.
McClay, K.R., Ellis, P.G., 1983. Deformation and recrystallization of pyrite. Mineralogical Magazine 47, 527–538.
McClenaghan, S.H., Lentz, D.R., Cabri, L.J., 2004. Abundance and speciation of gold in massive sulfides of the Bathurst mining camp. New Brunswick, Canada: Canadian Mineralogist 42, 851–871.
McClenaghan, S.H., Lentz, D.R., Martin, J., Diegor, W.G., 2009. Gold in the Brunswick No. 12 volcanogenic massive sulfide deposit, Bathurst Mining Camp, Canada: evidence from bulk ore analysis and laser ablation ICP-MS data on sulfide phases. Mineralium Deposita 44, 523–557.
Mercier-Langevin, P., Hannington, M.D., Dubé, B., Bécu, V., 2011. The gold content of volcanogenic massive sulfide deposits. Mineralium Deposita 46, 509–539.
Merkulova, M., Mathon, O., Glatzel, P., Rovezzi, M., Batanova, V., Marion, P., Boiron, M. C., Manceau, A., 2019. Revealing the chemical form of "invisible" gold in natural arsenian pyrite and arsenopyrite with high Energy-Resolution X-ray Absorption Spectroscopy: ACS Earth and Space. Chemistry v. 3 (9), 1905–1914.
Mikhlin, Y., Romanchenko, A., Likhacki, M., Karacharov, A., Erenburg, S., Trubina, S., 2011. Understanding the initial stages of metals precipitation: Nanoscale metallic and sulphide species of gold and silver on pyrite surfaces. Ore Geology Reviews 42, 47–54.
Atalaya Mining press release, 2021, Atalaya Mining PLC Announces Proyecto Masa Valverde Exploration Update - Junior Mining Network (https://www.juniorminingnetwork.com/junior-miner-news/press-releases/1789-tsx/aym/107866-atalaya-mining-plc-announces-proyecto-masa-valverde-exploration-update.html).
Morey, A.A., Tomkins, A.G., Bierlein, F.P., Weinberg, R.F., Davidson, G.J., 2008. Bimodal distribution of gold in pyrite and arsenopyrite: examples from the Archean Boorara and Bardoc shear systems. Yilgarn Craton, Western Australia: Economic Gelolgy 103, 599–614.
Morse, J.W., Luther, G.W., 1999. Chemical influences on trace metal-sulfide interactions in anoxic sediments. Geochimica et Cosmochimica Acta 63, 3373–3378.
Munhà, J., 1990, Metamorphic Evolution of the South Portuguese/Pulo Do Lobo Zone, in Dallmeyer, R., D., and Garcia E.M., eds., Pre-Mesozoic Geology of Iberia: Springer Berlin Heidelberg, Berlin, Heidelberg, p. 363-368.
Murowchick, J.B., Barnes, H.L., 1987. Effects of temperature and degree of supersaturation on pyrite morphology. American Mineralogist 72, 1241–1250.
Ohmoto, H., 1996. Formation of volcanogenic massive sulfide deposits: the Kuroko perspective. Ore Geology Reviews 10, 135–177.
Palenik, C.S., Ustunomiya, S., Reich, M., Kesler, S.E., Wang, L., Ewing, R.C., 2004. "Invisible" gold revealed: direct imagining of gold nanoparticles in a Carlin-type deposit. American Mineralogist 89, 1359–1366.
Pals, D.W., Spry, P.G., Chryssoulis, S., 2003. Invisible gold and tellurium in arsenic-rich pyrite from the Emperor gold deposit, Fiji: implications for gold distribution and deposition. Economic Geology 98, 479–493.
Pašava, J., Vymazalová, A., Tornos, F., 2007. PGE distribution in massive sulfide deposits of the Iberian Pyrite Belt. Mineralium Deposita 42, 309–314.
Petersen, S., Herzig, P.M., Hannington, M.D., 2000. Third dimension of a presently forming VMS deposit: TAG hydrothermalmound, Mid-Atlantic Ridge, 26°N. Mineralium Deposita 35, 233–259.
Piercey, S.J., 2011. The setting, style, and role of magmatism in the formation of volcanogenic massive sulfide deposits. Mineralium Deposita 46, 449–471.
Putnis, A., 2002. Mineral replacement reactions: from macroscopic observations to microscopic mechanisms. Mineralogical Magazine 66, 689–708.
Putnis, A., 2009. Mineral replacement reactions: Review in Mineral. Geochemistry 70, 87–124.
Reich, M., Kesler, S.E., Utsunomiya, S., Palenik, C.S., Chryssoulis, S.L., Ewing, R.C., 2005, Solubility of gold in arsenian pyrite: Geochimica et Cosmochimica Acta, v. 69 p. 2781–2796.
Reich, M., Utsunomiya, S., Kesler, S.E., Wang, L.M., Ewing, R.C., Becker, U., 2006, Thermal behaviour of metal nanoparticles in geologic materials: Geology, v. 34 p. 1033–1036.
Reich, M., Hough, R., Deditius, A., Utsunomiya, S., Ciobanu, C., Cook, N.J., 2011. Nanogeoscience in ore systems research: principles, methods and applications. Ore Geology Reviews 42, 1–5.
Revan, M.K., Genc, Y., Maslennikov, V.V., Maslennikov, S.P., Large, R.R., Danyushevsky, L.V., 2014. Mineralogy and trace-element geochemistry of sulfide minerals in hydrothermal chimneys from the Upper-Cretaceous VMS deposits of the Eastern Pontide orogenic belt (NE Turkey). Ore Geology Reviews 63, 129–149.
Sáez, R., Pascual, E., Toscano, M., Almodóvar, G.R., 1999. The Iberian type of volcano-sedimentary massive sulphide deposits. Mineralium Deposita 34, 549–570.
Sáez, R., Moreno, C., Gonzalez, F., Almodóvar, G.R., 2011. Black shales and massive sulfide deposits: causal or casual relationships? Insights from Rammelsberg, Tharsis, and Draa Sfar: Mineralium Deposita 46, 585–614.
Savage, K.S., Tingle, T.N., Peggy, A.D., Glenn, A.W., Bird, D., 2000. Arsenic speciation in pyrite and secondary weathering phases, Mother Lode Gold District, Tuolumne County, California. Applied Geochemistry 15, 1219–1244.
Serrati, S., Ferrini, V., Masi, U., Cabri, L.J., 2002. Trace-element distribucion in cassiterite and sulphides from Rubané and massive ores of the Corvo deposit, Portugal. The Canadian Mineralogist 40, 815–835.
Seward, T.M., Williams-Jones, A.E., Migdisov, A.A., 2014, The chemistry of metal transport and deposition by ore-forming hydrothermal fluids, in Turekian, K., and Holland, H., eds., Treatise on Geochemistry, 2nd edition, Elsevier, v. 13, p. 29-57.
Silva, J.B., Oliveira, J.T., Ribeiro, A., 1990, South Portuguese zone. Structural outline, in Dallmeyer, R.D., García, E.M., eds., Pre-Mesozoic Geology of Iberia, Springer, Berlin/Heidelberg, Germany. p. 348–362.
Simon, G., Huang, H., Penner-Hahn, J.E., Kesler, S.E., Kao, L.S., 1999. Oxidation state of gold and arsenic in gold-bearing arsenian pyrite. American Mineralogist 84, 1071–1079.
Solomon, M., 1976. Volcanic massive sulphide deposits and their host rocks: A review and an explanation. In: Wolf, K.H. (Ed.), Handbook of Strata-bound and Stratiform Ore Deposits, II: Regional Studies and Specific Deposits: Amstedam. Elsevier, pp. 1307–1328.
Southam, G., Saunders, J.A., 2005. The geomicrobiology of ore deposits: Economic Geology 100, 1067–1084.
Thompson, J.F.H., Lang, J.R., Stanley, C.R., 2001. Platinum group elements in alkaline porphyry deposits. Exploration and Mining in British Columbia Mines Branch Part B, British Columbia, pp. 57–64.
Torró, L., Benites, D., Vallance, J., Laurent, O., Ortiz-Benavente, B.A., Michou, C.C., Proenza, J.A., Fontboté, L., 2022. Trace element geochemistry of sphalerite and chalcopyrite in arc-hosted VMS deposits. Journal of Geochemical Exploration 232, 106882.
Tossell, J.A., Vaughan, D.J., Burdett, J.K., 1981. Pyrite, marcasite, and arsenopyrite type minerals: Crystal chemical and structural principles. Physics and Chemistry of Minerals 7, 177–184.
Trigub, A.L., Tagirov, B.R., Kvashnina, K.O., Chareev, D.A., Nickolsky, M.S., Shiryaev, A. A., Baranova, N.N., Kovalchuk, E.V., Mokhov, A.V., 2017. X-ray spectroscopy study of the chemical state of "invisible" Au in synthetic minerals in the Fe–As–S system. American Mineralogist 102, 1057–1065.
Vaughan, D.J., Craig, J.R., 1978. Mineral chemistry of metal sulfides. Cambridge Univ Press, Cambridge.
Wang, J.B., Deng, J.N., Zhang, J.H., Qin, K.Z., 1999. Massive sulphide deposits related to the volcano-passive continental margin in the Altay region. Acta Geological Sinica 73, 253–263.
Wang, K., Zhai, D., Liu, J., Wu, H., 2021. LA-ICP-MS trace element analysis of pyrite from the Dafang gold deposit. South China: Implications for ore genesis: Ore Geology Reviews 139, 104507.
Wright, J., Lentz, D.R., Rossiter, S., Garland, P., 2016, Analysis of Au-Ag Mineralization in the Caribou Base-Metal VMS Deposit, New Brunswick: Examination of Micro-Scale Inter- and Intra-Sulphide Distribution and Its Relation to Geometallurgy: Minerals, v. 6, p. 113.
Yamamoto, M., Kase, K., Tsutsumi, M., 1984. Fractionation of sulfur isotopes and selenium between coexisting sulfide minerals form the Beshi depsoit. Central Shikoku, Japan: Mineralium Deposita 19, 237–242.
Yang, S., Blum, N., Rahders, E., Zhang, Z., 1998. The nature of invisible gold in sulfides from the Xiangxi Au-Sb-W ore deposit in North-western Hunan. People's republic of China: The Canadian Mineralogist 36, 136l–l.
Yesares, L., Sáez, R., Nieto, J.M., Almodóvar, G.R., Gómez, C., Escobar, J.M., 2015. The Las Cruces deposit. Iberian Pyrite Belt, Spain: Ore Geology Review 66, 25–46.
Yesares, L., 2019, Mineralizaciones de oro en la Faja Pirítica Ibérica, in Moreno, C., Suárez, J., eds., La geología como soporte económico, histórico y social de la región. Actas de la II Jornada de Arqueología, Historia y Minería de la Faja Pirítica Ibérica, ISBN: 978-84-09-067 77-0.
Yuan, B., Yu, H., Yang, Y., Zhao, Y., Yang, J., Xu, Y., Lin, Z., Tang, X., 2018. Zone refinement related to the mineralization process as evidenced by mineralogy and

element geochemistry in a chimney fragment from the Southwest Indian Ridge at 49.6°E: Chemistry. Geology 482, 46–60.
Zachariáš, J., Fryda, J., Paterova, B., Mihaljevič, M., 2004. Arsenopyrite and As-bearing pyrite from the Roudny deposit. Bohemian Massif: Mineralogical Magazine 68, 31–46.
Zierenberg, R.A., Koski, R.A., Morton, J.L., Bouse, R.M., Shanks III, W.C., 1993. Genesis of massive sulfide deposits on a sediment-covered spreading center. Escanaba Though, Southern Gorda Ridge: Economic Geology 88, 2069–2098.